Climates of Warm Earth-like Planets I: 3-D Model Simulations

M.J. Way,[1,2] Anthony D. Del Genio,[1] Igor Aleinov,[1,3] Thomas L. Clune,[4] Maxwell Kelley,[1] and Nancy Y. Kiang[1]

[1]*NASA Goddard Institute for Space Studies, 2880 Broadway, New York, NY, 10025, USA*
[2]*Department of Physics and Astronomy, Uppsala University, Uppsala, 75120, Sweden*
[3]*Center for Climate Systems Research, Columbia University, New York, NY 10025, USA*
[4]*Global Modeling and Assimilation Office, NASA Goddard Space Flight Center, USA*

ABSTRACT

We present a large ensemble of simulations of an Earth-like world with increasing insolation and rotation rate. Unlike previous work utilizing idealized aquaplanet configurations we focus our simulations on modern Earth-like topography. The orbital period is the same as modern Earth, but with zero obliquity and eccentricity. The atmosphere is 1 bar N_2-dominated with CO_2=400 ppmv and CH_4=1 ppmv. The simulations include two types of oceans; one without ocean heat transport (OHT) between grid cells as has been commonly used in the exoplanet literature, while the other is a fully coupled dynamic bathtub type ocean. The dynamical regime transitions that occur as day length increases induce climate feedbacks producing cooler temperatures, first via the reduction of water vapor with increasing rotation period despite decreasing shortwave cooling by clouds, and then via decreasing water vapor and increasing shortwave cloud cooling, except at the highest insolations. Simulations without OHT are more sensitive to insolation changes for fast rotations while slower rotations are relatively insensitive to ocean choice. OHT runs with faster rotations tend to be similar with gyres transporting heat poleward making them warmer than those without OHT. For slower rotations OHT is directed equator-ward and no high latitude gyres are apparent. Uncertainties in cloud parameterization preclude a precise determination of habitability but do not affect robust aspects of exoplanet climate sensitivity. This is the first paper in a series that will investigate aspects of habitability in the simulations presented herein. The datasets from this study are opensource and publicly available.

1. INTRODUCTION

In recent years studies of the liquid water habitable zone for terrestrial exoplanets have mostly moved from the realm of 1-D (e.g. Kasting et al. 1993; Forget 1998; Selsis et al. 2007; Pierrehumbert & Gaidos 2011; Kopparapu et al. 2013; Popp et al. 2013; Kopparapu et al. 2014; Ramirez & Kaltenegger 2014) to fully 3-D coupled Atmophere and Ocean General Circulation Models (e.g. Merlis & Schneider 2010; Edson et al. 2011; Wolf & Toon 2013; Yang et al. 2013; Leconte et al. 2013b; Shields et al. 2014; Yang et al. 2014; Godolt et al. 2015; Kopparapu et al. 2016; Popp et al. 2016; Popp & Eggl 2017; Noda et al. 2017; Checlair et al. 2017; Boutle et al. 2017; Salameh et al. 2018). In general this has shown the value that 3-D modeling can bring to fully characterizing the climate state of a given world, the importance of cloud and ice albedo feedbacks and how different stellar types effect the habitable zone, among many other effects. On the other hand, because of computational limitations the majority of such 3-D studies have neglected the effect of lateral ocean heat transport (OHT). Recent exceptions include the work of Yang et al. (2013); Cullum et al. (2014); Hu & Yang (2014); Ferreira et al. (2014); Way et al. (2015, 2016); Fujii et al. (2017); Way & Georgakarakos (2017); Del Genio et al. (2018); Kilic et al. (2018) who utilized a fully coupled ocean, Charnay et al. (2013, 2017) who use a 2-layer ocean (Codron 2012) that mimics some aspects of a fully coupled ocean, and Godolt et al. (2015); Edson

Corresponding author: M.J. Way
Michael.J.Way@nasa.gov

et al. (2012); Kilic et al. (2017) who specified fixed lateral ocean heat transports perhaps first applied by Russell et al. (1985) for Earth climate studies.

One of the more stark representations of the effect that OHT has on such 3-D simulations was presented in the work of Hu & Yang (2014). Initial studies of tidally locked aquaplanet simulations around M-dwarfs demonstrated an "eye-ball" state where open water would appear in a circular region at the substellar point, but the rest of the planet would be covered in ice (e.g. Pierrehumbert 2011) even for high CO_2 concentrations. However, it is known that sea ice dynamics are intimately tied to OHT and has had an effect in simulations of snowball Earth studies (e.g. Yang et al. 2012a,b). Hu & Yang (2014) showed the "eyeball" state to be fictional and that a "lobster" state is a better reflection of reality, but it does require OHT.

To better understand the differences that OHT can have on climate dynamics we have analyzed a suite of three-dimensional (3D) General Circulation Model (GCM) simulations of an Earth-like planet on which two parameters, insolation and length of day, are varied over ranges suitable for surface habitability. The study includes a suite of simulations that both include and neglect OHT. Previous studies exploring insolation and rotation have been shown to have a range of effects on exoplanet climates (Yang et al. 2014; Kopparapu et al. 2016; Noda et al. 2017; Salameh et al. 2018), but at the same time OHT has been neglected in these studies. Our use of ROCKE-3D (Way et al. 2017) with OHT and its different treatment of clouds, convection, radiative transfer, dynamical core, and a host of other parameterized physics should help establish the generality of results where they overlap. However, direct comparison with previous work is also limited not only by the different treatment of OHT, but also because most previous work relied upon an aquaplanet setup, whereas we use an Earth-like land/sea mask. One may even consider a planet with Earth's present-day or past land-ocean distribution as a possibly more useful, demonstrably habitable, template for the rise of life as compared with aquaplanets. There is also an on-going debate in the community where some (Abbot et al. 2012) argue that it is not possible for an aquaplanet to support a climate stabilizing carbonate-silicate cycle, and those (Charnay et al. 2017) who argue otherwise. Until the debate is settled we believe it is a good idea to continue modeling the climates of both types of worlds.

2. METHODS

2.1. *Experimental Setup*

All simulations herein utilize ROCKE-3D (Way et al. 2017). ROCKE-3D is a generalized version of the Goddard Institute for Space Studies (GISS) ModelE2 (Schmidt et al. 2014) General Circulation Model (GCM). ROCKE-3D has been developed to allow a larger range of input variables than ModelE2 such as higher and lower atmospheric temperatures, rotation rates, atmospheric compositions and pressures.

We use a baseline version of ROCKE-3D known as Planet_1.0 which is described in detail in Way et al. (2017). In summary, ROCKE-3D is a Cartesian gridpoint model run at $4° \times 5°$ latitude $\times$ longitude resolution with 40 atmospheric layers and a top at 0.1 hPa. For this study the model is coupled to two different types of ocean with the same resolution as the atmosphere. The first is a "Q-flux" ocean (Russell et al. 1985), i.e., a thermodynamic mixed layer whose temperature is determined by radiative and turbulent energy exchange with the atmosphere. Lateral ocean heat transport is set to zero (Q-flux=0). The second ocean is a fully coupled dynamic ocean with 13 vertical layers down to a possible depth of 5000 m (Russell et al. 1995). However, the ocean is limited to a depth of 1360 meters for this study, which is the bottom of the 10th ocean layer in ROCKE-3D. This allows the model to come into radiative equilibrium faster than it would with the full-depth 5000m ModelE2 default Earth ocean.

The experiments use a baseline model that is similar to that used by ModelE2 for modern Earth climate studies, but differs from that model in several ways. At model start the following properties were specified:

- Planetary obliquity and eccentricity are zero. This avoids the additional complications of unraveling effects related to seasonal cycles as we see on Earth and Mars.

- Continental layout and land topography are roughly that of modern Earth. Some shallow ocean, seas and lake regions were replaced with land at locations that tend to freeze to the bottom at lower insolations. For example, land replaces the Baltic, Mediterranean, Red and Black Seas, and the Hudson Bay. The higher latitude seas freeze to the bottom at low insolations as a consequence of the zero obliquity used. Currently ROCKE-3D is unable to interactively change ocean gridboxes that freeze to the bottom to land ice.[1] The height of the

---

[1] The model will crash when this happens.

replacement land is set to the average height of the neighboring land grid cells. As well, some land is replaced by ocean where it may also cause problems in neighboring shallow continental shelf areas (e.g. between Australia and Indonesia). See Figure 8. A number of the default Earth boundary condition files were modified for these purposes (see Table 10), especially the river directions file which now contains river runoff direction for every grid cell. Runoff was also allowed for the Caspian Sea region, which otherwise does not have a runoff direction in the default Earth river directions file.

- The dynamic fully coupled ocean is a bathtub type ocean. Continental shelf regions are set to 591 meters in depth (ocean model level 8 of 13), while the rest of the ocean is set to 1360 meters (ocean model level 10 of 13). See Section 3.1 and Figure 8.

- Land albedo is set to 0.2 everywhere. The value is chosen to be the same as that used in the few non-aquaplanet simulations in Yang et al. (2014) to enable some inter-comparison. Those authors chose this value as a rough average albedo of a clay and sand mix. There is no glacial ice at model start, but snow is allowed to accumulate on land, which changes the albedo. Greenland and Antarctica maintain their present day topographies though they have no land-ice at model start. Note that the default land surface albedo in ROCKE-3D is spectrally flat.

- Lakes are allowed to shrink and expand, but excess run-off is transported downhill when the water exceeds the pre-defined lake height (also known as 'sill depth').

- Soil texture was chosen to be comparable to a "clay and sand" mix as in Yang et al. (2014) for the majority of simulations herein. The fractions for each particle class were not explicitly defined in that study, so we set them to 0.5 each. However, this corresponds to a soil texture classified as a sandy clay on the soil texture triangle (Jury et al. 1991), an arbitrary choice with regard to soil physical properties of porosity (saturated capacity) and water holding capacity. The latter is also known as "available water" after soil has drained from saturation, excluding water too tightly bound to soil particles to be available for life. For plants, that lower threshold of unavailable water is generally considered to be the "wilting point", ~ -15 bar matric potential, though in nature it may be more extreme, with microbes also able to extract water at lower matric potentials. At the hygroscopic point water is bound to soil particles by molecular forces and cannot be evaporated. To set lower and upper bounds on the potential availability of soil water (see Paper III[2] for details), we observed which simulations were very dry and very wet with the 50/50 clay/sand soil, and then we added to these end points more simulations with all sand soil (61D in Table 8) and all silt soil (22D & 72D in Table 8), which have, respectively, the lowest and highest water holding capacities. Texture-dependent soil physical properties are generally only estimated empirically, and representations differ among GCMs. Those used in ROCKE-3D's ground hydrology scheme for our chosen soil textures are listed in Table 1.

- No vegetation is included.

- Maximum land soil depth is 3.5 m uniformly around the globe, which is a restriction of the current ground hydrology scheme. Subsurface run-off is transported directly to the ocean. Solar radiative heating is allowed to penetrate to a soil depth of 3.5 meters. This choice is appropriate for the length of day on modern Earth. However, for the slower rotation periods that we simulate, a variable penetration depth consistent with the length of the day would be appropriate to implement in future versions of ROCKE-3D.

- Since the canonical habitable zone is the region around a star where an orbiting planet with an Earth-like atmosphere (i.e. N_2, CO_2, CH_4, H_2O) could maintain surface liquid water (e.g. Hart 1979; Kasting et al. 1993) we prescribe present day Earth surface atmospheric pressure (984 millibars), with N_2 the major constituent and prescribed spatially uniform concentrations of the minor radiatively active constituents $CO_2 = 400$ ppmv[3] and $CH_4 = 1$ ppmv and a modern Earth water vapor profile at model start. O_3 is set to zero in line with most previous exoplanet studies, with the exception of Godolt et al. (2015) who retain O_3 in most of their simulations. Aerosols (i.e., hazes from photochemical, volcanic, or dust- or ocean-stirring processes) are also not explicitly included, although their presence as nuclei for cloud formation is implicit.

---

[2] Kiang et al. (2018)
[3] Parts Per Million by Volume.

Table 1. Soil textures used in experiments

Soil Type	Soil Water Content[a]	Hygroscopic water[b]	Available Water[c]
50/50% clay/sand	1699.062238324	377.958232212	1322.8538127422
100% sand	1378.847624922	108.488011098	1270.3596138239
100% silt	1879.292321277	237.973701763	1641.3186195135

[a] ROCKE-3D saturated water content for 3.5 m deep soil in units of kg m^{-2}. The large number of significant digits is required for accuracy when you consider that the ice-free land surface area is $\sim$1.30577 x 10^{14} m^2.

[b] ROCKE-3D hygroscopic water for 3.5 m deep soil in kg m^{-2}.

[c] ROCKE-3D maximum available water soil water for 3.5 m deep soil in kg m^{-2}.

- H_2O is the only other radiatively active constituent besides CO_2 and CH_4. Its concentration varies in space and time in accordance with the parameterized convection, condensation and evaporation physics and dynamical transport in the model. The effect of variable H_2O on atmospheric mass is neglected. The maximum monthly mean gridbox specific humidity (mass concentration of H_2O) in the lowest altitude model layer in the runs with the warmest surface temperatures were found to be $\lesssim$0.1 in any gridbox. Thus, our neglect of H_2O mass is a $\sim$10% or smaller effect in our simulations.

ROCKE-3D was run first at Earth's present day sidereal rotation period t_{rot} (X001) = 1 and insolation (S0) = 1360.67 W m^{-2}, and then in a series of experiments at higher insolation and longer sidereal days; see Tables 2, 3). Simulations were generally conducted for surface temperatures that remain lower than 400 K. This is close to the upper temperature limit for accurate calculations with our radiation scheme SOCRATES (Edwards & Slingo 1996; Edwards 1996) which uses HITRAN2012 (Rothman et al. 2013). See Goldblatt et al. (2013) for details on the accuracy of HITRAN2008 versus HITEMP2010, although our use of HITRAN 2012 may imply even smaller differences with the HITEMP database.

The suite of simulations are summarized in Tables 2 and 3.

3. RESULTS

3.1. *Sensitivity to Ocean Model*

Most previous exoplanet GCM studies have utilized a static thermodynamic ocean with no ocean heat transport, because of its computational efficiency (e.g. Yang et al. 2014; Merlis & Schneider 2010; Shields et al. 2013; Wolf & Toon 2015; Turbet et al. 2016). In this section we examine the effect that a dynamic fully coupled ocean with ocean heat transport has on planetary climate and impressions of liquid water habitable zone extent.

Figure 1a shows the global mean surface temperature of ROCKE-3D as a function of insolation for sidereal day lengths of 1 Earth day to 256 Earth days for a 100 meter deep thermodynamic Q-flux=0 ocean. Our results are qualitatively similar to those of Yang et al. (2014) who use the NCAR CAM3[4] in an aquaplanet configuration (their Figure 1). Recall again that we use a modern Earth-like topography, not an aquaplanet. Mean surface temperature increases sharply with insolation at present day Earth's day length (X001) but is less sensitive as the day length increases. There are several quantitative differences between ROCKE-3D and the CAM models used by Yang et al. (2014) as far as one can compare our Earth-like land/sea mask to their aquaplanet configuration. For the Q-flux=0 runs ROCKE-3D is more sensitive to increasing insolation at present day Earth's day length (X001) and at 16 sidereal days (X016). The trend reverses for day lengths of 64 d (X064) and larger. Consequently, the ROCKE-3D simulations divide clearly into two classes: moderate to rapidly rotating planets with high sensitivity to insolation, and slowly rotating planets with low sensitivity, as opposed to the CAM simulations (Fig. 1 of Yang et al. (2014)) for which sensitivity is a more continuously decreasing function of rotation period. We return to this question below.

---

[4] National Center for Atmospheric Research Community Atmospheric Model version 3

Table 2. Q-flux=0 (zero ocean heat transport) simulation summary[1]

Insolation[2]	Rotation Period(d)[3]								
S0X	X001	X002	X004	X008	X016	X032	X064	X128	X256
1.0/1360.67	x,t,c	x	x	x	x	x	x	x	x
1.1/1501.80	x,t	x	x	x	x,c	x	x	x	x
1.2/1638.40	x,t	x	x	x	x	x	x,c	x	x
1.3/1774.90	n,t	x	x	x	x	x	x	x,c	x
1.4/1911.40		x	n	x	x	x	x	x	x
1.5/2047.90					n	x	x	x	x
1.7/2321.00						x	x	x	x
1.9/2594.00						x	x	x	x
2.1/2867.10						n	x	x	x
2.3/3140.00							x	x	x
2.5/3413.25							x	x	x
2.7/3686.30							x	x	n
2.9/3959.37							x	n	
3.1/4232.40							n	n	

[1]x: Run completed and is in net radiative and hydrological balance. n: Ran for several model years, but crashed before reaching net radiative balance. c: Run with all convective cloud condensate converted to precipitation. t: Run with different cloud tuning parameters. See Section 3.2 for details on 'c' and 't.'

[2]Present day Earth solar insolation (S0X=1.0) is set to 1360.67 W m^{-2}. Subsequent S0X use S0=1365.3 W m^{-2} multiplied by X. For example, S0X=1.1 × 1365.3 = 1501.8

[3]Rotation: values are in multiples of Earth length sidereal days (d). Sidereal=Solar Day equivalents are 1=1, 16=16.7, 32=34.97, 64=76.6, 128=191, 256=848.
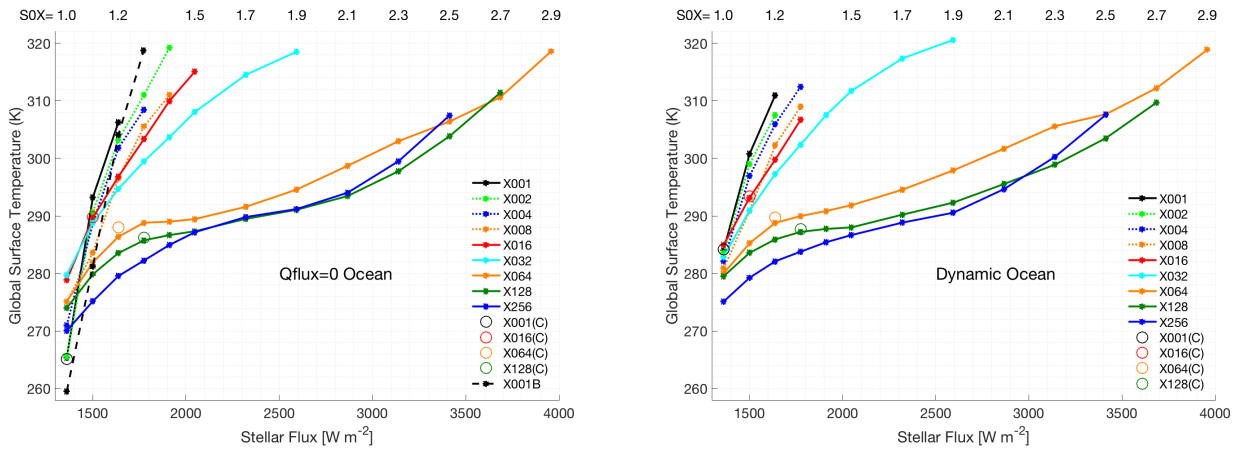

Figure 1. Global mean surface temperature for ROCKE-3D as a function of insolation at different rotation periods for thermodynamic ocean simulations (a, left) and dynamic fully coupled ocean (b, right). Solid curves and dots show results from the baseline model at 10% increments above the modern Earth insolation value and 20% increments above S0X=1.5. Open circles are for sensitivity tests with no vertical transport of convective condensate. The dashed curve is for an alternate model version with the same physics but using different settings of free parameters to adjust the model to global radiative balance.

Table 3. Fully coupled dynamic ocean simulation summary[1]

Insolation	Rotation Period(d)								
S0X	X001	X002	X004	X008	X016	X032	X064	X128	X256
1.0	x,c	x	x	x	x	x	x	x	x
1.1	x	x	x	x	x,c	x	x	x	x
1.2	x	x	x	x	x	x	x,c	x	x
1.3	n	n	x	x	x	x	x	x,c	x
1.4				x	x	x	x	x	x
1.5				n	n	x	x	x	x
1.7						x	x	x	x
1.9						x	x	x	x
2.1						x	x	x	x
2.3							x	x	x
2.5							x	x	x
2.7							x	x	n
2.9							x	n	n
3.1							n	n	n

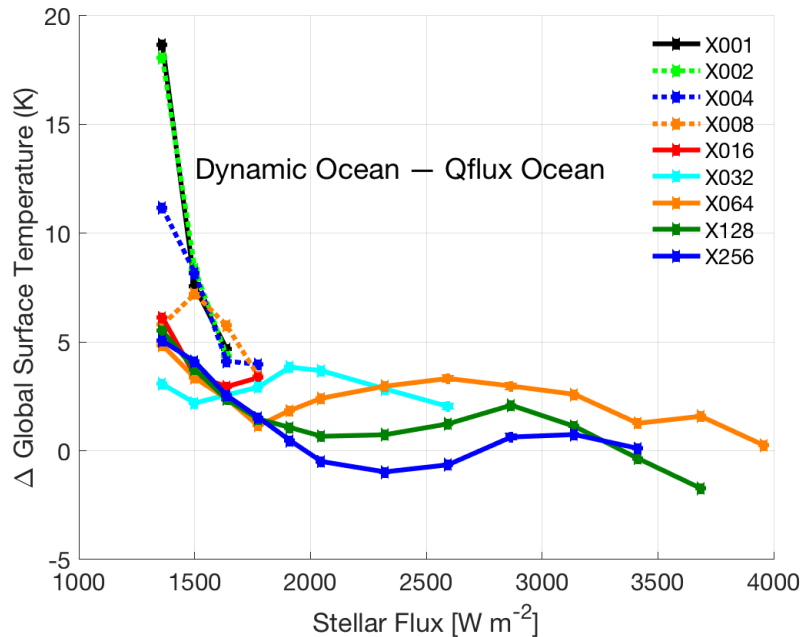[1] See Table 2 caption for column and row descriptions.

Figure 2. Global mean surface temperature differences when subtracting the Q-flux=0 mean temperature from that of the dynamic ocean.

Our results for Earth's rotation period (X001) can also be compared with those in Figure 1 of Wolf & Toon (2015) who plot climate sensitivity for their CAM3 & CAM4 results, but also for the LMDG[5] results of Leconte et al. (2013a).

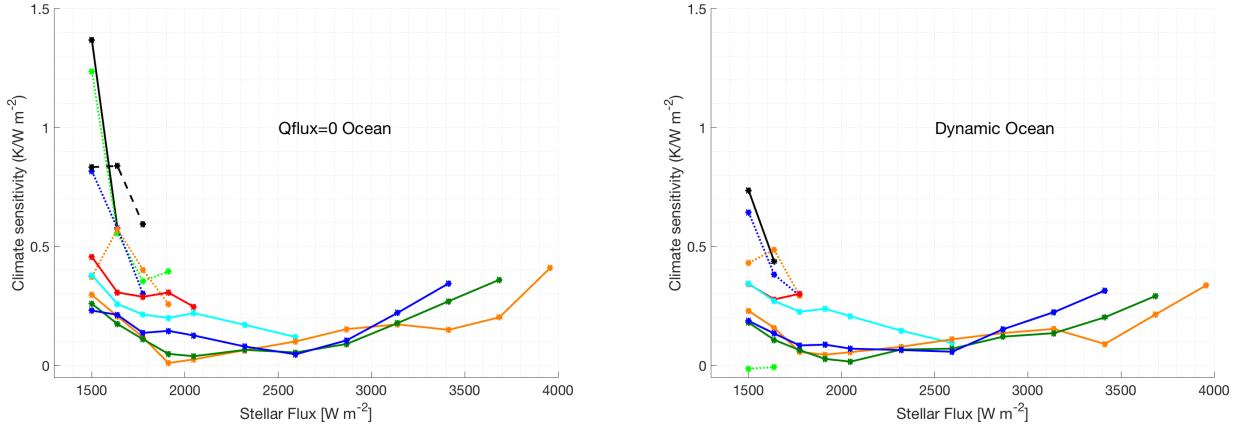[5] Laboratoire de Météorologie Dynamique Generic

Figure 3. Climate Sensitivity for Q-flux=0 (a, left) and Dynamic Ocean runs (b, right).

ROCKE-3D is much more sensitive than the CAM3 and CAM4 results to a 10% increase in insolation (S0X=1.1), but much less sensitive than the LMDG GCM, which has a large warming for insolation increases of 5-10%. For a 20% increase (S0X=1.2, the only other simulation comparable in Wolf & Toon 2015) ROCKE-3D is less sensitive than CAM4 because CAM4 warms dramatically at 11-12% insolation increase while ROCKE-3D does not.

Figure 1b is identical to Figure 1a but for a dynamic fully coupled ocean. The results for day lengths of 64 d (X064) and longer are very similar to those for the thermodynamic ocean case. However, for the X001 day lengths the dynamic ocean model is significantly warmer (see Figure 2), and considerably less sensitive to insolation increases.

The climate sensitivity to changes in sunlight is usually expressed as the response of surface temperature to the absorbed sunlight rather than the insolation itself (see, e.g. Eqn. 2 of Wolf & Toon 2015). This quantity is shown in Figure 3 for both types of ocean. Climate sensitivity is highest for the fastest rotators and most weakly irradiated planets and is very small for the slow rotators regardless of absorbed sunlight. The dynamic ocean simulations have a markedly lower climate sensitivity than the Q-flux=0 simulations for fast rotation periods.

To explain these differences among models, Figures 5 & 6 shows the extent to which the two different ocean types affect aspects of the planetary (Bond) albedo, ocean ice fractional extent, and cloudiness at different levels of the model. The upper panels of Figure 5 show that at the lower insolation values, the rapidly and slowly rotating planets behave in opposite fashion: planetary albedo initially decreases with insolation in the shorter day length simulations (more so for the Q-flux=0 ocean) but increases with insolation for longer day lengths. At higher insolations, all simulations exhibit increasing planetary albedo as insolation increases. This is partly explained by the sensitivity of the ocean ice fraction to insolation, rotation, and ocean dynamics. The zero obliquity of this Earth-like world allows ocean ice to grow considerably at higher latitudes when the insolation is low, but the ice melts (and thus the surface albedo decreases) when either insolation increases or the length of day increases. The latter dependence occurs because heat is more efficiently transported poleward on slowly rotating planets with broader Hadley cells (Del Genio & Suozzo 1987). The higher ocean ice fractions for the Q-flux=0 versus dynamic ocean at lower insolations clearly points to the role that a dynamic ocean plays in equator to pole heat transport.

The increase in planetary albedo with insolation for the longer day lengths is due to the now well-documented substellar cloud bank as shown in previous 3D model simulations (e.g. Yang et al. 2014). This occurs because moist convection at low latitudes increasingly transports water vapor and cloud particles upward as insolation increases. The convection itself occupies a small area but produces more extensive anvil clouds at the levels where water vapor and cloud particles detrain into the environment (Fu et al. 1990). On Earth, the anvil clouds are primarily a feature of the upper troposphere. This is also true in the current experiments at low insolation. Interestingly, though, as insolation increases convection depth seems to decrease, because high cloud cover decreases as middle level cloud cover increases in Figure 6. The latter clouds apparently dominate the optical thickness and thus the dependence of planetary albedo on insolation. Low level clouds decrease with increasing insolation at low insolation values, similar to how 3D Earth climate models respond to 21st Century increases in anthropogenic greenhouse gas concentrations (Klein et al. 2017). However, at higher insolation low cloud cover tends to increase with insolation instead. For example, in Figure 4 the
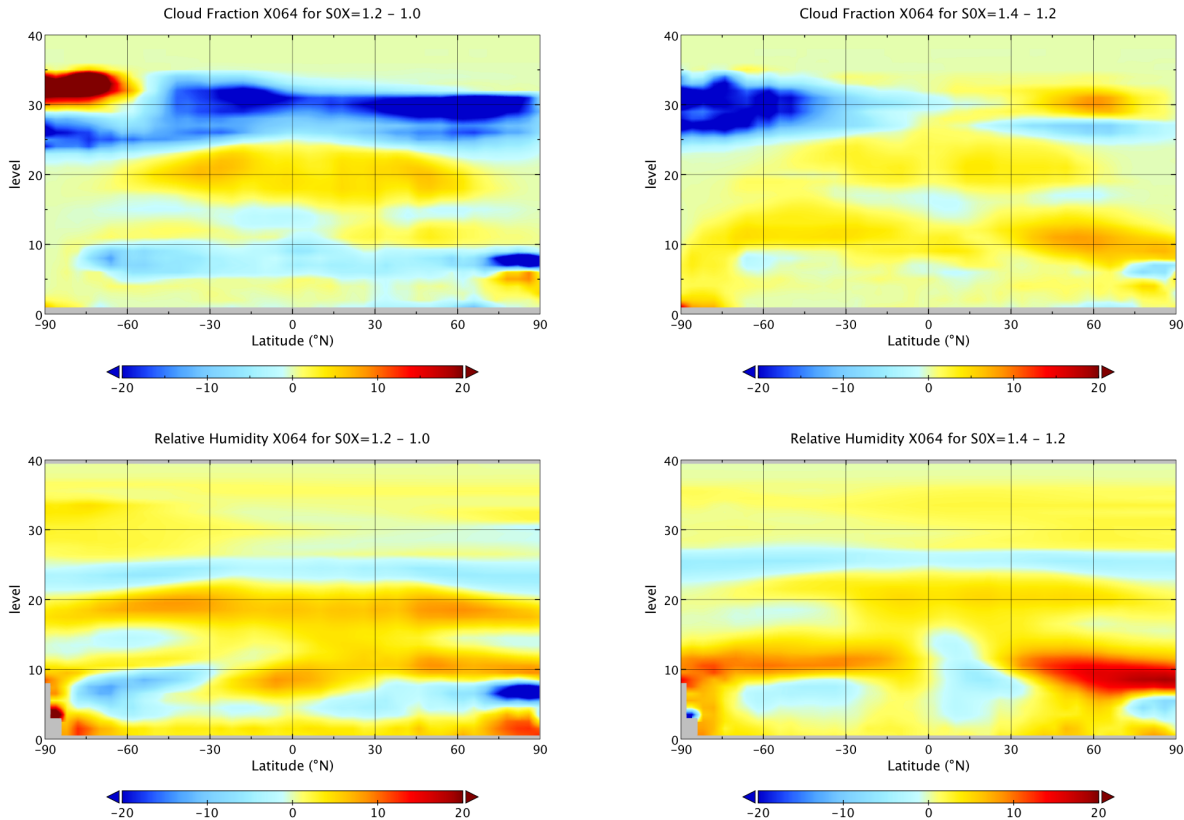
Figure 4. Total cloud fraction (top) and relative humidity (bottom) for the difference between two low insolation runs (left) and higher insolation runs (right). These are all from a single rotation period of X064. X-axes are all in degrees of latitude, while the y-axes are all in units of atmospheric levels (1-40).

decrease in low clouds from insolation values of 1.0 to 1.2 and the increase from 1.2 to 1.4, are both related to relative humidity, mostly at high latitudes. This make sense because there is less shallow convection at high latitudes.

The ocean dynamics are strongly tied to the rotation rate of the planet. This can most clearly be shown by looking at a range of rotation rates for a fixed insolation as shown in Figure 7. At the faster rotations (X001–X004) the ocean current are very Earth-like, with gyres in the northern hemisphere in both ocean basins and an Antarctic circumpolar current in the southern mid-latitudes. The gyres clearly transport heat poleward, as the real Gulf Stream does on Earth, but because there is more sea ice on this planet due to the zero obliquity the transport is very important at low S0X and fast rotation. The dynamic ocean runs have less sea ice than their Q-flux=0 equivalents and thus the dynamic ocean climates are generally warmer as described earlier and shown in Figure 2. The trend goes up until about X016, by which time the Hadley cell now stretches to the pole and so the ocean heat transport is directed equator-ward with no gyres. By this rotation the sea ice is already gone so the addition of ocean heat transport doesn't do very much, hence the insensitivity of the results to ocean heat transport at slower rotations.

Despite the advantages of a dynamic ocean limitations exist as well. The ROCKE-3D ocean model utilizes the Gent & McWilliams (1990) Earth-specific parameterization for mesoscale mixing by unresolved eddies, which is appropriate to the quasi-geostrophic ocean flow on a rapidly rotating planet. Little information exists about the behavior of mesoscale ocean eddies in the slowly rotating dynamical regime, although several studies have explored the rotation dependence of overall ocean heat transport (Farneti & Vallis 2011; Cullum et al. 2014). However, in a Proxima Centauri b simulation with ROCKE-3D it was found that changing the mesoscale diffusivity had little effect (Del Genio et al. 2018). As mentioned previously, the fully coupled ocean simulations have only two depths: 591m near continent boundaries and 1360m elsewhere (see Figure 8). This allows the model to come into thermodynamic equilibrium faster than it would if we used all 13 ocean model layers to 5000m, and hence lowers the total computational time per simulation. The results of Russell et al. (2013) and Hu & Yang (2014) suggest that ocean heat transport increases with ocean depth, with
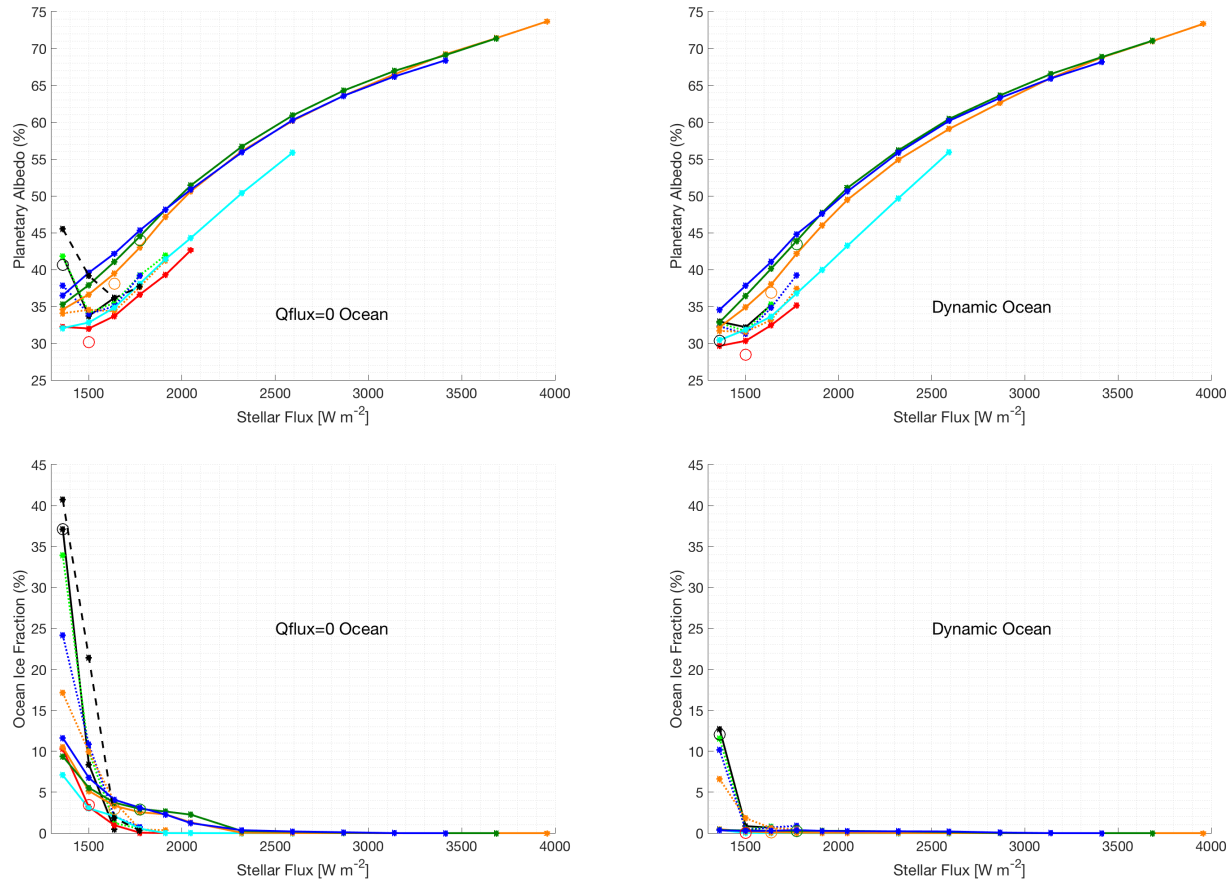
Figure 5. Planetary Albedo (top) and Ocean Ice Fraction (bottom) for Q-flux=0 (left) and Dynamic Ocean runs (right).

concomitant effects on climate, although this is likely to be partly compensated by increased atmospheric transport (Stone 1978). Ocean bottom topography, the location of continents, and the steepness of continental boundaries all influence ocean circulation and thus heat transports. Likewise, salinity is specified as that of Earth's ocean, which need not be the case on another planet. This has implications for the density-driven component of the ocean circulation and especially the freezing temperature (see Del Genio et al. 2018), which in turn affects albedo. Finally, the impact of tides, which are strongly correlated with the size/mass and distance of the Earth's moon, is neglected in ROCKE-3D. These are not strictly limitations, since exoplanets can be expected to have a large variety of ocean depths and either no moons or moons of varying size and distance, and these will likely be unconstrained by observations for the foreseeable future. It may however be a consideration for deep paleo-Earth studies simulating time periods when the moon was closer to Earth and the tides were higher.

3.2. *Cloud parameterization sensitivity*

Clouds are considered the most uncertain aspect of GCMs, accounting for much of the inter-model spread in estimates of the global climate sensitivity of Earth to increases in greenhouse gas concentrations (Vial et al. 2013). A coupled ocean-atmosphere climate model must be in global top-of-atmosphere radiation balance at something close to Earth's observed surface temperature in order to be used for climate change applications. Given the uncertainties in GCM cloud parameterizations, free parameters are usually adjusted within reasonable limits to achieve balance while not overly compromising other aspects of the simulated climate (Mauritsen et al. 2012). For exoplanets, no effective observational constraints exist, nor is there any guarantee that a model developed for modern Earth will reach radiative balance on its own. Thus adjustments of the free parameters may be necessary. Here we consider two cloud uncertainties to illustrate the limitations of 3-D studies of exoplanets and the conclusions that can be drawn despite the limitations.

The Yang et al. (2014) baseline model has a global surface temperature of 287 K for Earth's rotation period (their Figure 1c), remarkably close to Earth's observed surface temperature. Given that the Yang et al. (2014) runs are
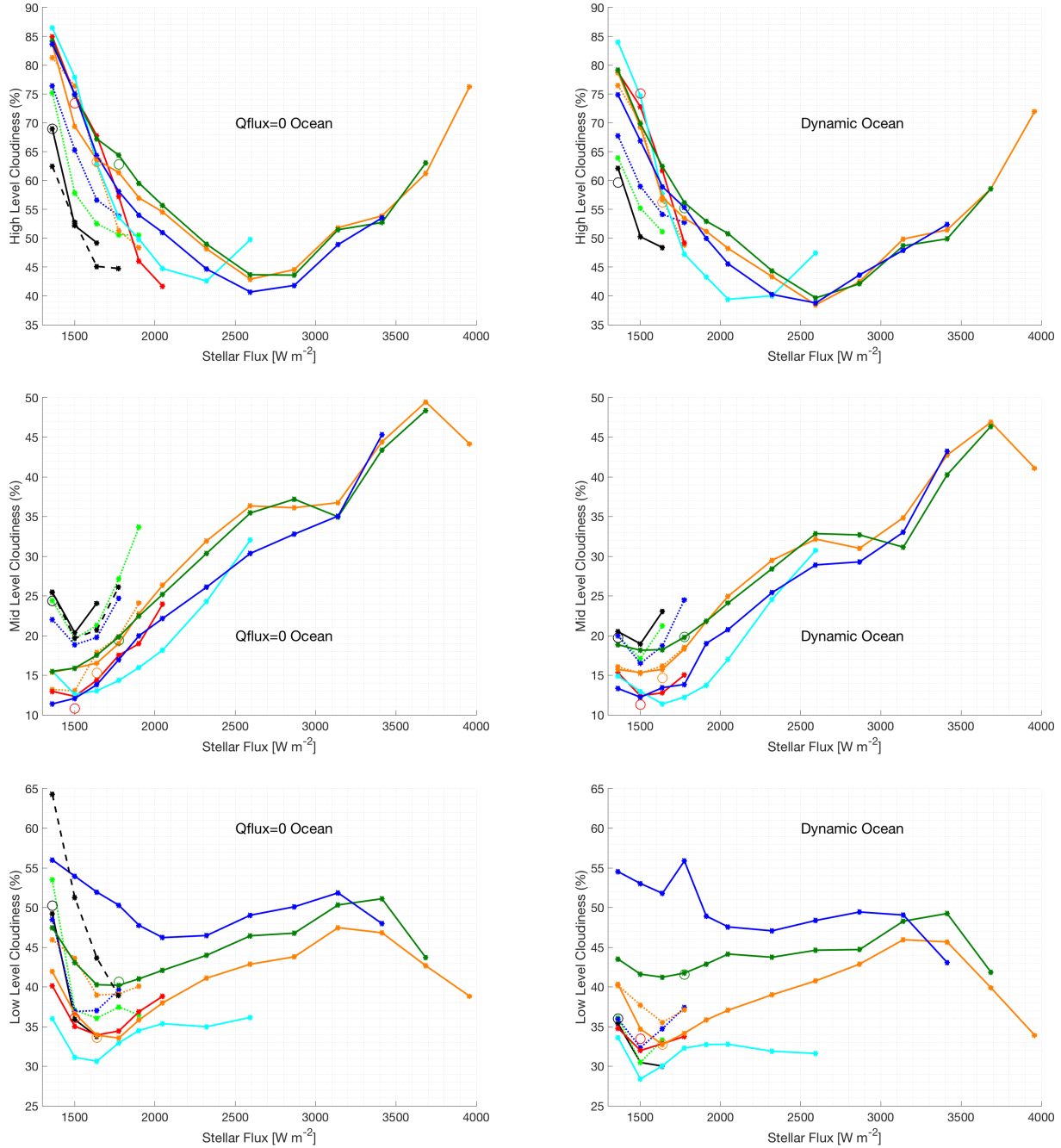
Figure 6. Cloud Fractions at highest level (top), middle level (middle) and bottom level (bottom) for Q-flux=0 (left) and Dynamic Ocean runs (right). Note: the y-axes have different values from top to bottom.

aquaplanets while those herein are Earth-like it should not be surprising that ROCKE3D's Q-flux=0 run (see Table 9) is cooler (265 K) while our dynamic ocean simulation (Table 8) has a temperature of 284 K. The reason for the difference between these temperatures and that of modern Earth is that the planet being simulated is clearly not Earth (e.g., it has no aerosols or vegetation). Most importantly, the planet has zero obliquity and eccentricity. Earth's present day obliquity warms the poles and cools the tropics. We expect the first of these to be more important because it reduces sea ice and snow cover and decreases the Bond albedo, at least for planets in the quasi-geostrophic dynamical regime that have large equator-pole temperature gradients (Del Genio 2013; Madeleine et al. 2014). Thus, although the global temperature of our idealized planet cannot be constrained, if such a zero-obliquity planet existed, it would
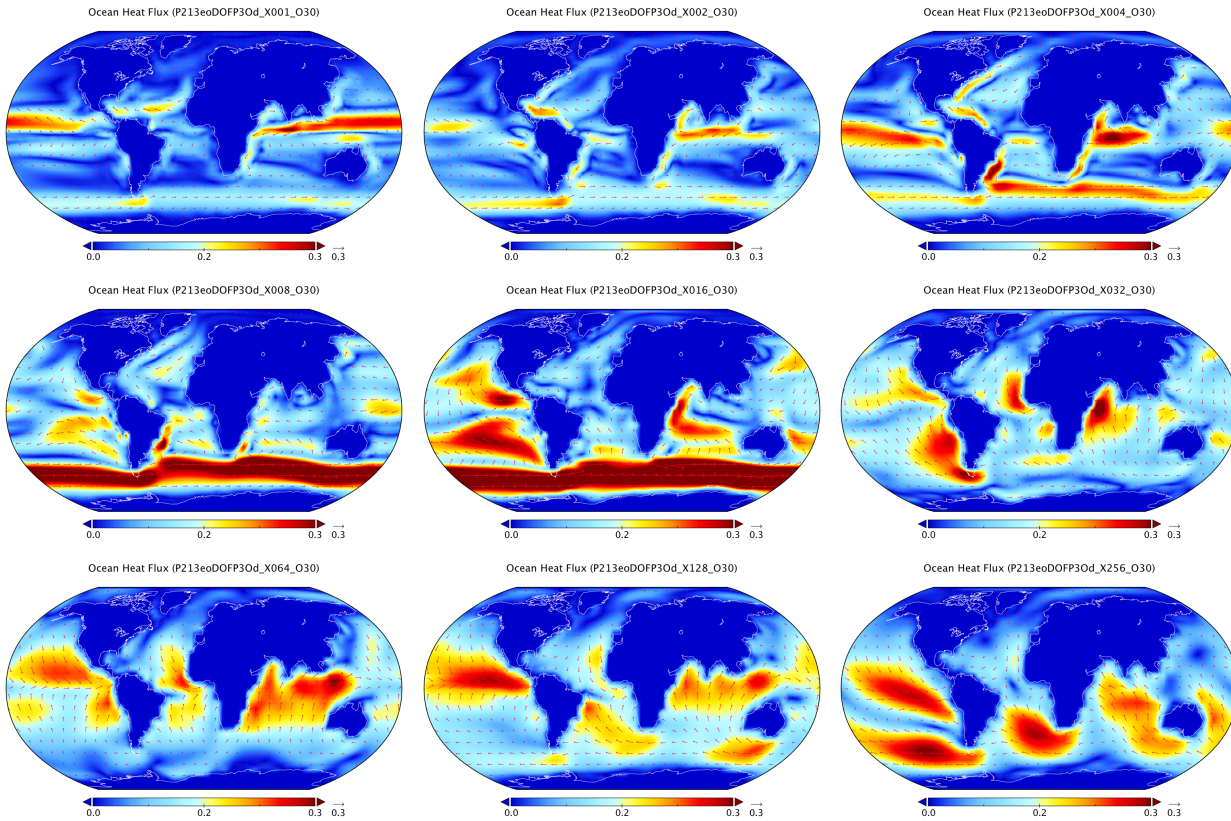
Figure 7. Meridional plus zonal ocean heat flux ($\sqrt{\text{Meridional}^2 + \text{Zonal}^2}$) in units of 10^{15} Watts. These are 9 runs at fixed insolation of S0X=1.2 from sidereal length of day = X001 (1 x Earth), all the way up to X256 sidereal days in length.

likely be colder than Earth. The warmer temperature of the dynamic ocean model reflects the role that ocean thermal inertia and heat transport play in limiting sea ice extent.

To test the sensitivity of the Q-flux=0 model temperature to the choice of model tuning, we created an alternate version of our baseline planet (See legend for 't' in Table 2 and X001B in Figure 1a) with free parameters in the cloud parameterization chosen differently but still within the range of uncertainty for modern Earth to produce radiation balance at a different climatic state. Specifically, we changed the values of two parameters that determine the threshold relative humidity at which stratiform clouds begin to form (one for free troposphere clouds, one for boundary layer clouds) and thus the cloud fraction. We also changed a parameter that affects how quickly small cloud ice crystals grow into large snowflakes by gravitational coalescence and precipitate out of the cloud, thus altering the cloud's ice water content and optical thickness.

Figure 1a (X001B, dashed black line) shows the global mean surface temperature of this alternate model as a function of insolation for Earth's rotation period, for comparison with the baseline model (X001, solid black line). The alternate model has a global mean surface temperature of 259.5 K for Earth's insolation (S0X=1.0) compared to the baseline model's 265.4 K (a difference of $\sim$ 6 K), but its sensitivity to insolation change is fairly similar to that of the baseline model (see Figure 3a). The result is that this planet can sustain a 20% increase in insolation and remain only slightly warmer (11K) than the baseline model does for a 10% increase in insolation. This implies that model-based estimates of the edges of the habitable zone, whether 1-D or 3-D, are only weak constraints on where habitable planets may be found, since model clouds can be tuned to give a variety of climates.

The more important question is whether any definitive statements can be made at all about the effects of clouds on exoplanet climates. The primary finding of Yang et al. (2014) is that a planet can remain habitable at much higher values of insolation if it is slowly rotating than if it is rapidly rotating. This occurs because at rotation rates slow enough (long day lengths) for significant day-night temperature differences to arise, convergence on the dayside leads to rising motion and moist convection that produces a shield of high, optically thick clouds that limit warming there and stabilize the planet's climate. The fact that ROCKE-3D produces qualitatively similar behavior (Figure 1) is an
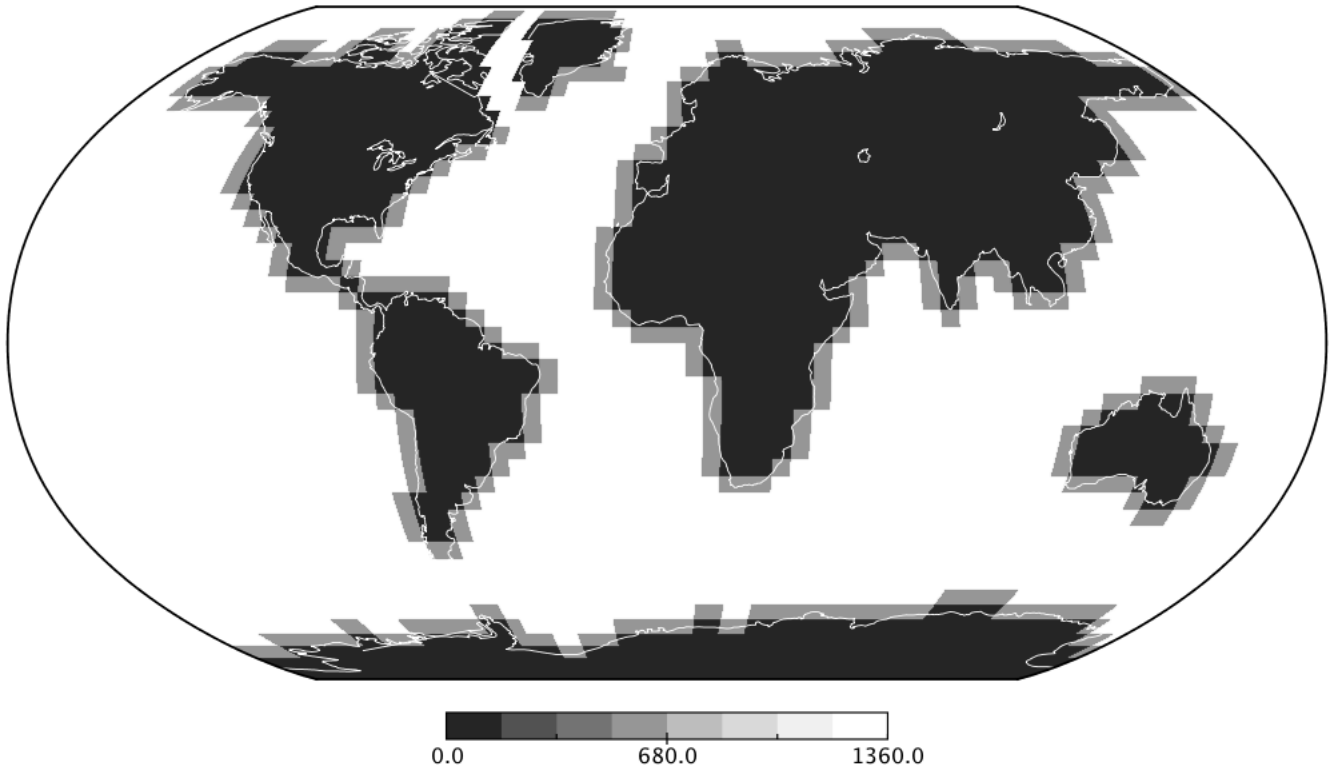
Figure 8. Ocean bathymetry. Gridboxes at continent boundaries have an ocean depth of 591m (light gray), while the rest of the ocean is 1360m (white). Some seas/bays like the Hudson Bay, Baltic Sea, Black Sea, Caspian Sea, and Mediterranean Sea have been filled in with land (black). We have removed the island chain from Australia to south east Asia, much of the Malay and Kamchatka peninsulas, and islands like Indonesia, Japan, Madagascar, Malaysia, New Zealand and the Carribbean have been replaced with ocean. The channel between Greenland and the northern Nunavut islands (e.g. Ellesmere) and Drake's Passage has also been opened slightly.

encouraging sign that this might be a robust feature of planetary climates. In our own Solar System, this process may be relevant to the question of whether ancient Venus was habitable (Way et al. 2016).

On the other hand, moist convection is one of the most challenging and uncertain aspects of terrestrial climate models (Del Genio 2015). The dayside cloud that stabilizes the climate at slow rotation is the end result of a series of parameterized cloud and convection processes: A decision to initiate convection, an assumption about the updraft mass flux and vertical velocity, and an assumption about how much of the condensate that forms in the updraft is transported upward and detrained along with saturated updraft vapor. ROCKE-3D does this by diagnosing an updraft speed profile, assuming particle size distributions and size-dependent fall speeds, and interactively calculating the fraction of the condensate that precipitates vs. being transported upward to form thick anvil cloud (Del Genio et al. 2005, 2007). Each of these steps introduces uncertainty, e.g., the parameterization in the baseline model overestimates the ice carried upward by convective events (Elsaesser et al. 2017). Since ∼80 percent of the cloud ice that results from deep convection in the terrestrial GCM is the result of upward transport of particles rather than in-situ ice formation from supersaturated air, it is reasonable to ask whether the rotation dependence of surface temperature is parameterization-dependent.

To address this, we performed another sensitivity test in which we assume that all condensate in the convective updraft precipitates. We denote such runs "convective condensate precipitates" in Tables 2, 3, 8 and 9. Thus, middle and upper level clouds can only form from supersaturated vapor detrained by convective updrafts or created by large-scale resolved upward motion. We conducted one simulation for four rotation periods at different insolations (open

circles in Figure 1). The simulations without upward transport of condensate are predictably warmer, but only by a couple of degrees, than the simulations with the full convective physics, independent of rotation period. That is, cloud that forms in-situ from the vapor detrained by the updraft or the resolved upward motion is primarily what stabilizes the temperature. Insensitivity of the results to this type of structural modification, rather than simply a parameter change, strengthens the case for the conclusions of Yang et al. (2014).
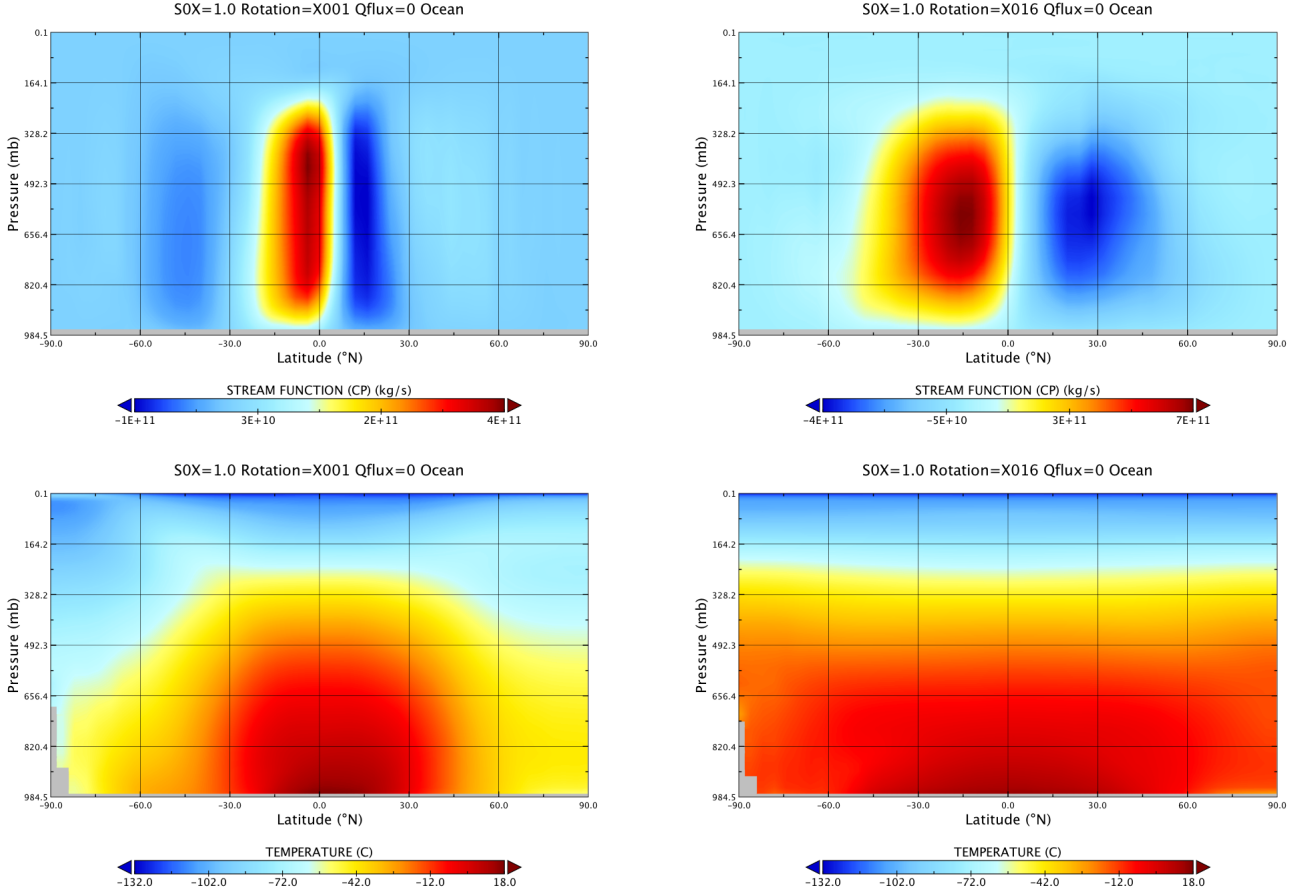

Figure 9. Top panels: model stream function diagnostic showing increase in Hadley Cell size and decrease in number from Rotations X001 to X016. Bottom panels: The increase in the size of the Hadley cell transports more heat to higher latitudes. This effect is seen in the latitudinal temperature differences between X001 and X016. This is also seen in the decrease in the amount of high latitude Sea Ice (Ocean Ice Fraction) in Figure 5 in the lower left panel between the X001 and X016 simulations for the same insolation (in this case S0X=1.0).

This supports the idea that the fundamental behavior operating in all these models is not the details of the cloud physics but the interaction between the dynamics and radiation. The transition from a very sensitive to a weakly sensitive climate as day length increases depends on two transitions in dynamical regime that determine how heat is transported. The first is from the quasi-geostrophic regime characteristic of rapidly rotating planets to the quasi-barotropic regime of more slowly rotating planets. This transition has been well studied for rocky planets (Williams & Holloway 1982; Del Genio & Suozzo 1987; Del Genio et al. 1993; Allison et al. 1995; Navarra & Boccaletti 2002; Showman et al. 2013). Both regimes are dominated by poleward heat transport. In the quasi-geostrophic regime this is accomplished by a Hadley circulation at low latitudes, with mean rising motion near the equator and sinking motion in the subtropics, and by baroclinically unstable eddies that produce low and high pressure centers and fronts at higher latitudes. In the quasi-barotropic regime, the Hadley cell spans most latitudes and dominates the global heat transport. This transition occurs approximately when the Rossby radius of deformation (the spatial scale of rapid baroclinic eddy growth) approaches the size of the planet (Del Genio et al. 1993; Edson et al. 2011; Showman

et al. 2013). It differentiates the atmospheric circulations of Earth and Mars from those of Venus and Titan. Our simulations with 1 d rotation period are in the quasi-geostrophic regime, while the 16 d period simulations are in the quasi-barotropic regime. In Figure 9 we show how the Hadley cell changes in size when going between these regimes and how it clearly effects the surface temperatures and ocean ice fraction at high latitudes (see Figure 5).

The second transition is from a circulation that transports heat poleward to a diurnally-driven circulation that transports heat from a dayside region of rising motion to a nightside region of sinking motion, with day-night transport both over the poles and across the terminators. The day-night circulation has been explored by Joshi et al. (1997); Joshi (2003); Yang et al. (2013) for synchronously rotating planets and by Yang et al. (2014) for slowly rotating but asynchronous planets. In our simulations the transition appears to occur between 32 d and 64 d rotation period. This can be understood by considering the radiative relaxation time scale $t_{rad} = pc_pT/(gF)$, where p is pressure, c_p the specific heat at constant pressure, T the temperature, g the acceleration of gravity, and F the emitted thermal flux to space. For Earth heated at 1 AU by the Sun $t_{rad} \sim 1$–2 months, depending on the pressure level one chooses for the calculation. When the length of the solar day $t_{sol} << t_{rad}$, day-night temperature differences are small, and equator-pole temperature gradients drive the circulation. When $t_{sol} \gtrsim t_{rad}$, day-night temperature contrasts become important and the circulation develops a strong diurnally-driven component. This regime transition occurs in the 32–64 d rotation interval (for which t_{sol} is only slightly longer than the rotation period) for the planets we simulate. Showman et al. (2015) invoke a similar argument to define the boundary between circulations characteristic of weakly irradiated jovian planets and strongly irradiated hot Jupiters.

These changing transport patterns among the three dynamical regimes matter for habitability because they determine where optically thick clouds form and thus where sunlight is more strongly reflected. They also matter for the water cycle because of their effect on precipitation patterns, as we will explore in future papers in this series. Despite uncertainties in parameterized cloud physics, the only requirement of the cloud/convection physics is that thick clouds form where large scale upward motion is prevalent. This basic behavior should be model-independent for any mass flux cumulus parameterization, since it requires only that rising air adiabatically cool and eventually saturate.
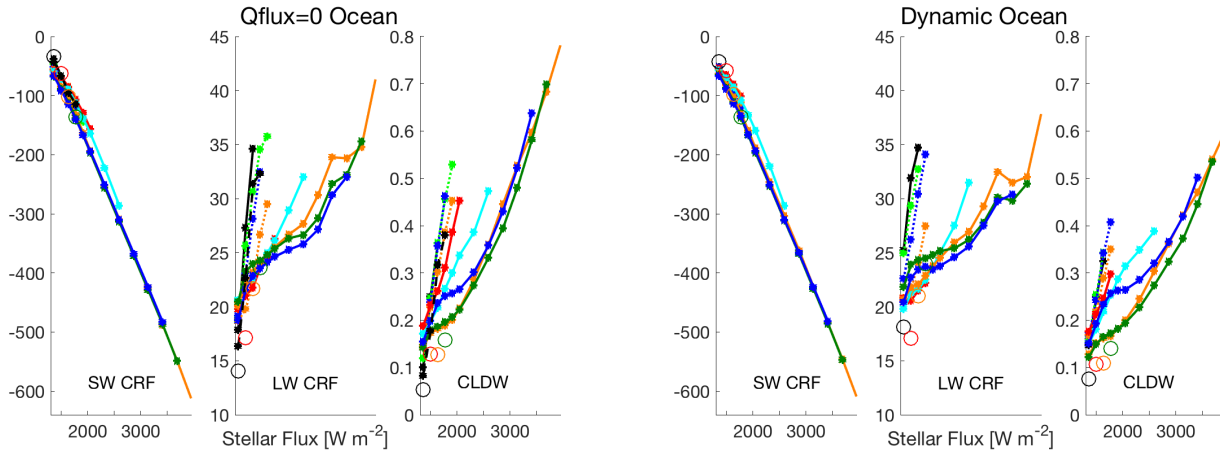
Figure 10. Cloud Radiative Forcing (CRF) for the short wave (SW) and long wave (LW) in W m^{-2} along with the column-integrated cloud water (CLDW) in kg m^{-2}.

Figure 10 shows the global mean shortwave (SW) and longwave (LW) cloud radiative forcing (CRF), as well as the column-integrated cloud condensed water (liquid + ice; CLDW) as a function of incident solar flux S_o and rotation period. CRF measures the effect of clouds on a planet's top-of-atmosphere radiation budget (e.g., Cess et al. 1990). We use the convention that downward/upward fluxes (i.e., heating/cooling of the planet) are positive/negative and define the absorbed SW flux:

$$Q = S_o(1 - A)/4 \tag{1}$$

where A is the planetary (Bond) albedo, and the emitted LW flux:

$$F = \sigma T_e^4 \tag{2}$$

where T_e is the equilibrium temperature.

Letting subscript c indicate the fluxes that would exist in clear skies (calculated by a separate offline call to the radiation parameterization that ignores the clouds), and subscript o the fluxes that exist in overcast skies, we define:

$$SWCRF^6 = Q - Q_c = [fQ_o + (1 - f)Q_c] - Q_c = fS_o(A_c - A_o)/4 \tag{3}$$

$$LWCRF^7 = F_c - F = f(F_c - F_o) = \sigma f(T_{ec}^4 - T_{eo}^4) \tag{4}$$

where f is the cloud fractional area.

Positive/negative values of CRF indicate heating/warming by clouds, respectively. SWCRF < 0 because clouds are more reflective than the clear sky and most surfaces and thus make a planet cooler than it would be without clouds, while LWCRF > 0 because clouds absorb upwelling thermal radiation and re-radiate it at a lower temperature, producing greenhouse warming. Note that CRF depends not only on the coverage and properties of clouds but also on the properties of the clear-sky atmosphere and planet surface through the terms Q_c and F_c. Thus changes in CRF in response to a climate forcing such as an increase in incident solar flux capture the cloud feedback only in the context of the accompanying clear sky changes rather than isolating the cloud feedback itself (Soden & Held 2006).

Figure 10 shows that SWCRF increases monotonically in magnitude with incident solar flux and is somewhat stronger for the slowly rotating planets, as expected. Much of the insolation dependence reflects the increase in S_o itself, but for a doubling of S_o, SWCRF increases by about a factor of 3, indicating that cloud fraction and/or the albedo difference between overcast and clear skies increases with insolation as well. Cloud vertically integrated water (CLDW) actually increases more slowly with insolation for the slowly rotating planets, but this is misleading because the clouds on the slow rotators are much denser on the dayside, where they can contribute to SWCRF. LWCRF is smaller than SWCRF and increases slowly as incident solar flux increases This does not appear to be due to increasing cloud height, given that high cloud cover decreases and middle level cloud cover increases with insolation, at least for the lower insolation values (Figure 6). Furthermore, the high cloud decrease exceeds the middle cloud increase, so cloud fraction does not appear to be the cause. Instead, the similarity of the LWCRF and cloud water dependences on temperature and insolation suggest that cloud opacity, and its implications for the radiating temperature contrast between cloud and clear skies, controls the LWCRF behavior. The net result of the SWCRF and LWCRF behavior is that the clouds exert a net cooling effect on the climate that becomes stronger as the incident flux increases, i.e., by this simple measure the net cloud feedback is negative.

Rotation period does not directly affect temperature, so the cooling of the planet as rotation slows in Figure 1 must be the result of climate feedbacks that occur as the dynamical regime changes in response to the changing rotation. Figure 11 shows the LWCRF, SWCRF, and column integrated water vapor as a function of rotation period for different values of S0X. From 1 d to 16 d period, SW cloud cooling generally weakens, though this is partly offset by an increase in LW cloud warming. Furthermore, sea ice decreases with increasing rotation period as the Hadley cell expands (Figure 9). Thus, neither cloud nor sea ice feedbacks can explain the generally cooler temperatures and lower climate sensitivity as rotation slows. Instead, the dramatic decrease in water vapor with increasing rotation period ($> 50\%$ for most values of S0X) reduces the greenhouse effect of the clear sky atmosphere. Water vapor continues to decrease with longer rotation period for periods up to 128 d, but SWCRF becomes increasingly negative and LWCRF slightly less positive. All three feedbacks are thus negative, consistent with the large separation in temperature in Figure 1 between the more rapidly and more slowly rotating planets.

4. DISCUSSION

Our results support the conclusions of previous work (e.g. Yang et al. 2014) that rapidly rotating planets like Earth are much more susceptible to a runaway greenhouse than are slowly rotating planets at high insolations. As mentioned above, some of the differences between the work herein and previous results may be related to the different GCMs

---

[6] Short Wave Cloud Radiative Forcing

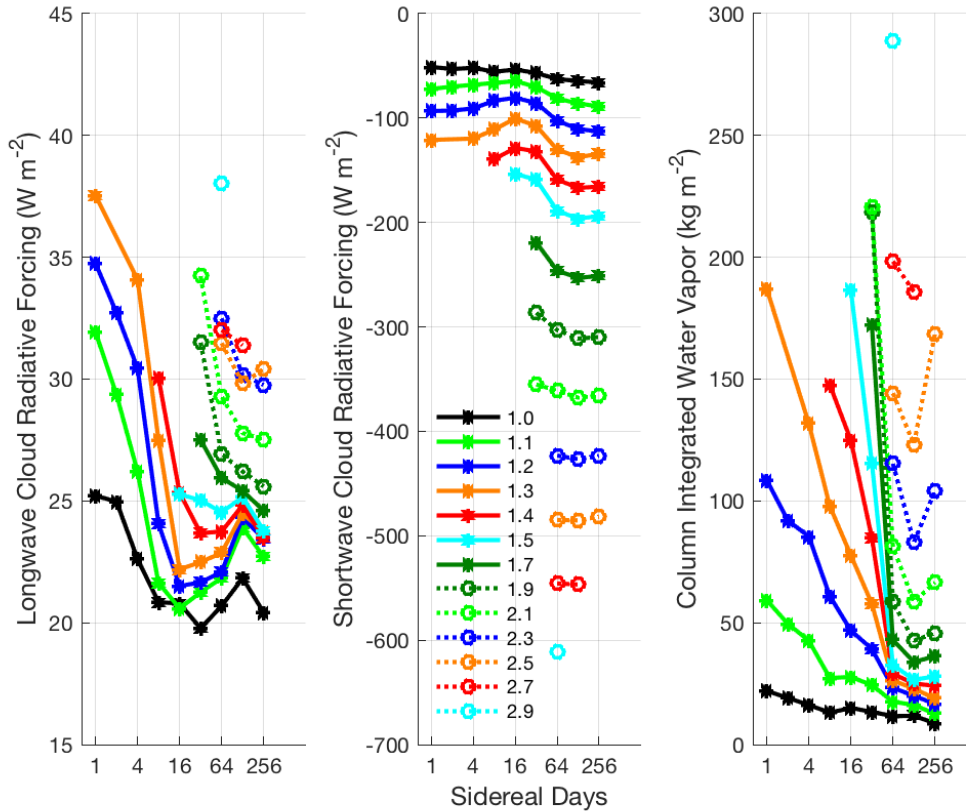[7] Long Wave Cloud Radiative Forcing

Figure 11. (Left) Longwave Cloud Radiative Forcing (CRF), (center) Shortwave CRF, and (right) column integrated water vapor as a function of rotation period for the dynamic ocean simulations for different S0X values.

being used, the types of oceans (dynamic ocean versus thermodynamic ocean), and an Earth-like topography and land/sea mask versus aquaplanet configurations.

As mentioned in Section 2.1 ROCKE-3D does not yet use high temperature line lists, nor does it account for the effect of water vapor mass on the dynamics, so beyond the fact that ROCKE-3D lies within the range of previous GCM studies that concluded that the inner edge of the habitable zone must be significantly closer to the Sun than 1-D models estimate, we cannot estimate a precise inner edge location.

On the other hand one can look at diagnostics of water vapor transported into the stratosphere, where it can potentially be photodissociated, leading to hydrogen escape and onset of the moist greenhouse, a more conservative definition of the inner edge of the habitable zone. To that end in Figure 12 we show water vapor molar concentration in the highest model layer for the grid cell with the largest value (A & B) and the mean in the highest layer (C & D) to investigate whether any of our simulations begin to approach the moist greenhouse limit of Kasting et al. (1993), i.e. $f(H_2O)=3\times10^{-3}$. Figure 12A shows that for the highest insolation runs of most rotations with a Q-flux=0 ocean the stratosphere exceeds the 3×10^{-3} limit in a given grid cell whereas the mean Figure 12C does not in general. With the dynamic ocean in Figure 12B most of the high insolation rapidly rotating planets (rotations <X032) almost reach the moist greenhouse state, whereas for the slower rotating models where S0X>2.9 they exceed the 3×10^{-3} limit for the maximum grid cell value. However, if one takes the mean of the highest layer Figure 12D then one finds they are roughly similar to the Q-flux=0 runs in Figure 12B.

We have shown that the representation of ocean dynamics is just as important a consideration for extreme exoplanet climates as is the representation of radiation, particularly so for rapidly rotating planets as shown in the 1 d – 32 d cases herein. It should be noted that ROCKE-3D cannot actually reach the runaway greenhouse definition of the inner edge of the habitable zone for terrestrial worlds, unlike in many of the works cited above. The radiative transfer in ROCKE-3D cannot accurately calculate heating rates for temperatures over 400K. In addition, the dynamics begins
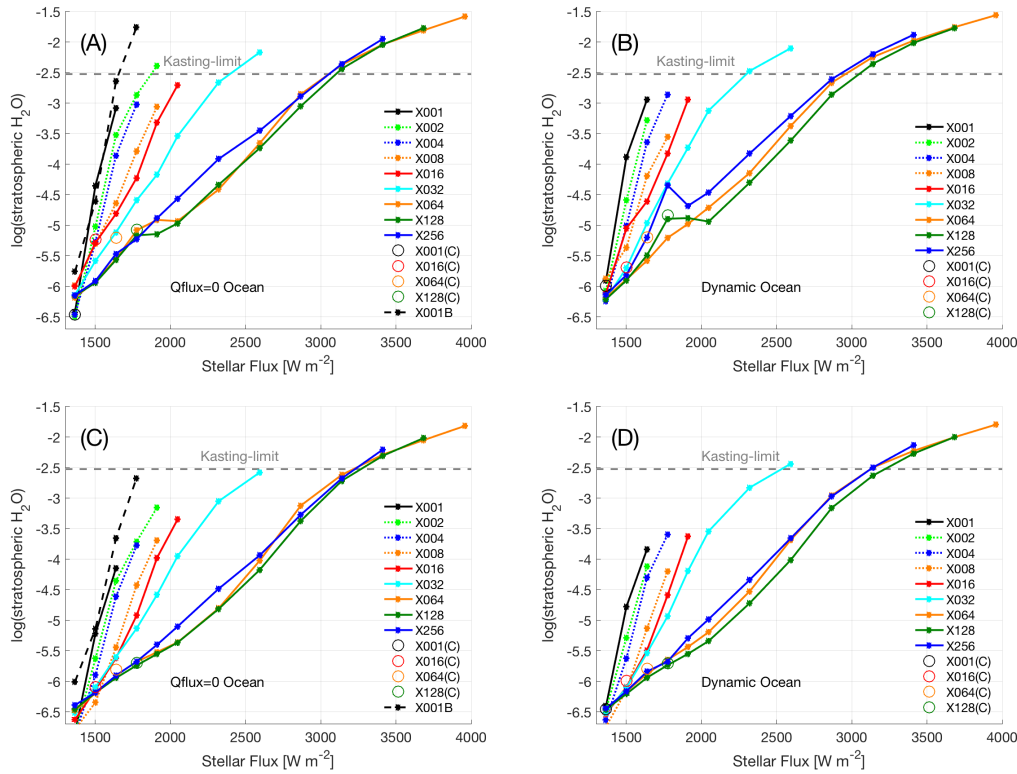
Figure 12. Stratospheric water vapor content for Q-flux=0 ocean runs (A/C, left) and Dynamic Ocean runs (B/D, right). Y-axis is the $\log_{10}$ of the specific humidity at 0.1 hPa for H_2O/Air (kg/kg). A & B are values for the grid cell with the largest value at the highest layer in each simulation whereas C & D are the mean at the highest layer.

to lose accuracy when water vapor becomes more than 10% of the mass of the atmosphere and begins to significantly affect pressure gradients and the assumed ideal gas behavior of the atmosphere. When water vapor starts to becomes a non-negligible fraction of the atmospheric mass it also becomes important to be able to adjust the atmospheric constants such as the atmospheric mass, and heat capacity at constant pressure and volume, which ROCKE-3D is not presently capable of doing.

Future papers in this series will address different habitability metrics such as that of Spiegel et al. (2008) and others related to water availability that are crucial to life on present day Earth.

The data from this paper is open source and at publication time will be made available on the ROCKE-3D NCCS[8] data portal website: https://portal.nccs.nasa.gov/GISS_modelE/ROCKE-3D An additional copy of the files will also be made available at https://archive.org/details/Climates_of_Warm_Earth_like_Planets

[8] NASA Center for Climate Simulation

Table 4. Calendar day lengths 1 & 2

Name	1 day [1]	2 days [2]
Mean solar day	1.000000	2.005329
Sidereal Rotation Period	0.997268	1.994379
Sidereal Orbital Period	365.000000	365.256369
Solar Days per year	365.000000	182.142857

[1]Modern Earth Sidereal Day (ESD) length.

[2]Twice the length of modern ESD length.

Table 5. Calendars for day lengths 1 & 2

	Modern Earth			2 x Modern Earth[1]			120 day calendar[2]		
Month	day length	first day	last day	length	first	last	length	first	last
January	32	1	32	16	1	16	11	1	11
February	29	33	61	14	17	30	09	12	20
March	31	62	92	16	31	46	10	21	30
April	30	93	122	15	47	61	10	31	40
May	30	123	152	15	62	76	10	41	50
June	29	153	181	14	77	90	10	51	60
July	30	182	211	15	91	105	09	61	69
August	31	212	242	15	106	120	10	70	79
September	29	243	271	15	121	135	10	80	89
October	31	272	302	16	136	151	10	90	99
November	31	303	333	15	152	166	10	100	109
December	32	334	365	16	167	182	11	110	120

[1]Calendar for when sidereal day length is twice modern Earth's.

[2]Calendar for all sidereal day lengths greater than two Earth sidereal days.

APPENDIX

A. CALENDAR

As detailed in Way et al. (2017) ROCKE-3D uses a 120 day calendar system when the numbers of days per year is less than 120 days. There is an option for overriding this feature, but it was not utilized for the simulations herein. For this reason we are publishing details from the calendar in use for these simulations in Tables 4, 5 and 6. The 120 day default calendar goes into effect for any simulations with sidereal day lengths longer than 2 Earth sidereal days.

ROCKE-3D places the calendar output into a runtime text file with additional details of the run as it moves forward in time. For all runs (regardless of the calendar in use) the Longitude at Periapsis is fixed to 282.9°.

The movement of the substellar point month-by-month is an intuitive way for the reader to understand the implications of the 120 day calendar. In Table 7 we show an example of the movement of the substellar point in each monthly output for each of the runs. We do not show results for rotation rates faster than X032 as the substellar point is too smeared out over monthly output to be visually meaningful.

Table 6. Additional calendar day lengths in multiples of Earth sidereal days

Name	4 days	8 days	16 days	32 days	64 days	128 days	256 days
Mean solar day	4.032799	8.156210	16.684998	34.967671	77.339399	196.228155	848.066511
Sidereal Rotation Period	3.988759	7.978059	15.956119	31.912537	63.825075	127.650149	255.300299
Sidereal Orbital Period	365.256369	-	-	-	-	-	-
Solar Days per year	90.571429	44.782609	21.891304	10.445545	4.722772	1.861386	0.430693

Table 7. Substellar point in monthly output

Month	X032	X064	X128	X256
January				
February				
March				
April				
May				
June				
July				
August				
September				
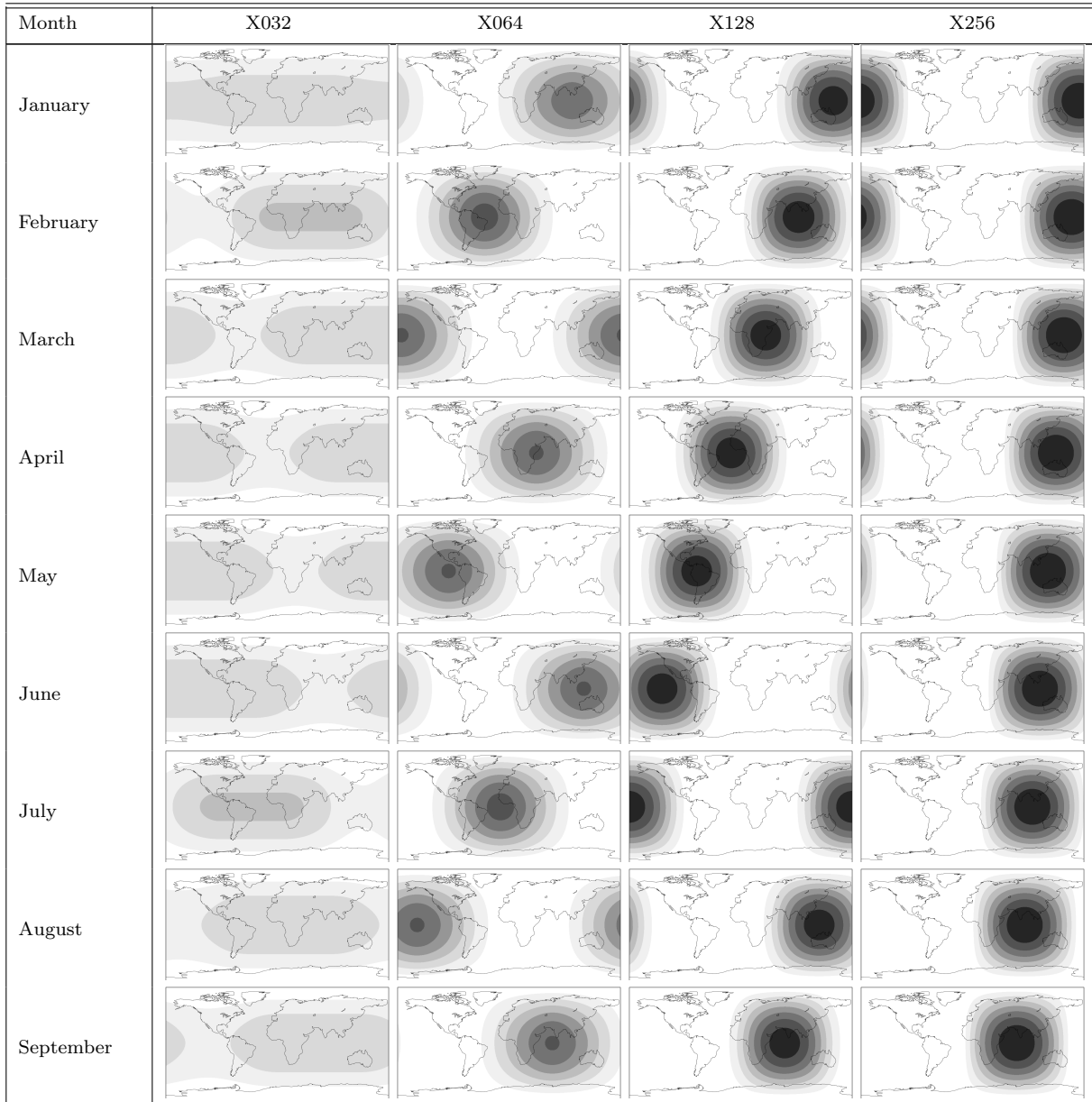
Table 7 continued on next page

Table 7 (continued)

Month	X032	X064	X128	X256
October				
November				
December				
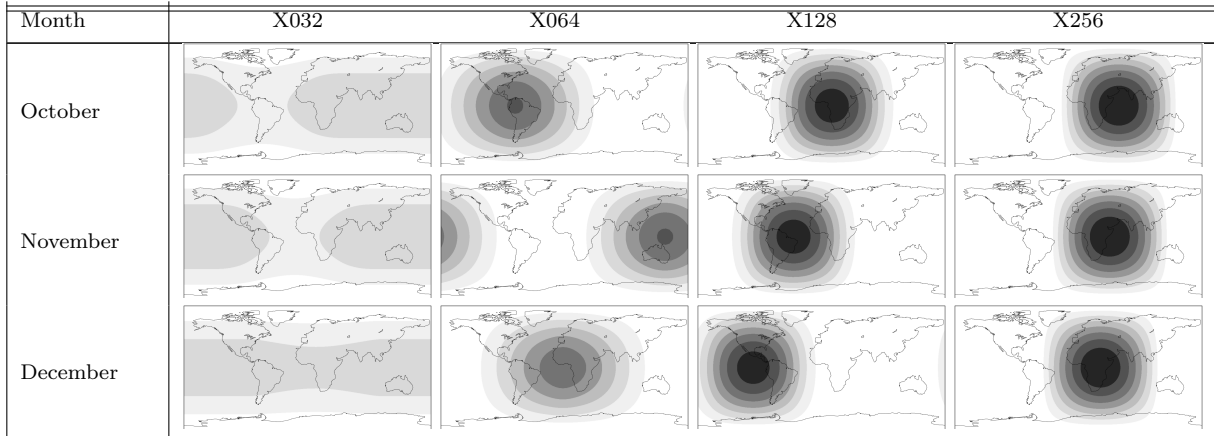
B. EQUILIBRIUM

To determine whether a GCM under a particular forcing (be that via differences in concentrations of radiatively active gases or via changes in insolation) has reached equilibrium, one typically looks at the energy balance at the top of the atmosphere. For ROCKE-3D we prefer the net radiative balance to be within $\pm$ 0.2 W m^{-2} of zero, which is as good as or better than most current Earth climate models (Forster et al. 2013). For the simulations of water metrics to be discussed in Paper II we need to also look at surface and sub-surface water diagnostics over land to ensure that they are in steady state, which can take longer than is required to achieve energy balance. Figures 13 & 14 show two examples from different insolation and day length regimes.

Figure 13. S0X=1.0 with sidereal day length set to 4 days (X004). Left (a) from top to bottom y-axes are net radiative balance in W m^{-2}, surface temperature in Celsius,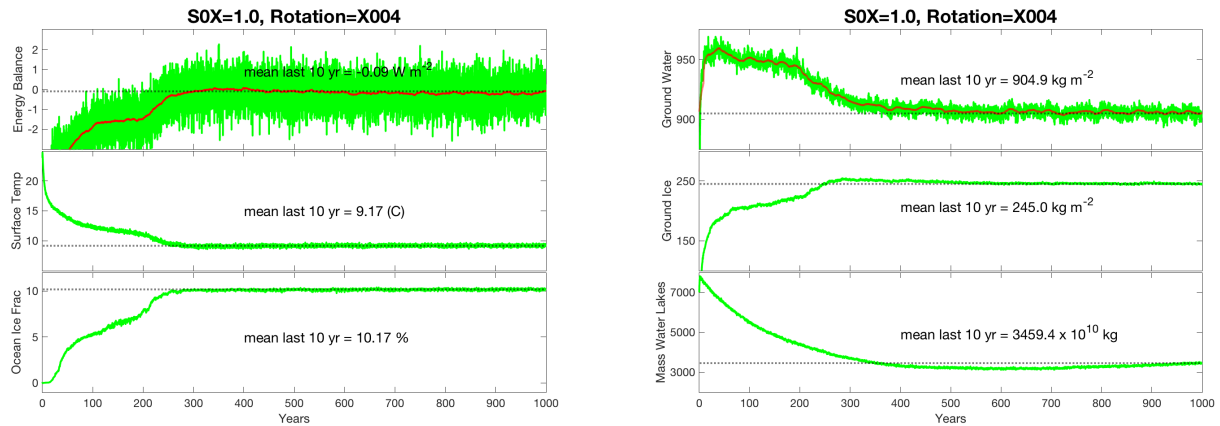 and ocean ice fraction in total percentage of ocean area. Right (b) from top to bottom y-axes are total global ground water amounts in kg m^{-2}, total ground ice in kg m^{-2} and the total mass of water in lakes and rivers in kg.

In Figure 13a it is apparent that it takes the model approximately 300 years to come into energy balance. As expected both the global mean surface temperature and ocean ice fraction also reach a stable state about the same time. The latter can have a large effect given the high albedo of ocean ice versus ocean liquid water. In Figure 13b one can see that the ground water (liquid and ice) takes a bit longer to stabilize at around 500 years. The ground ice also stabilizes around 500 years. The last diagnostic in Figure 13b is the mass of water in lakes and rivers. One can see that at model start it is far from stability, and it takes nearly 500 model years for it to begin to stabilize. This is partly because of the different non-modern-Earth topography used given that we start with modern Earth topographic ground initial conditions. There is also the fact that the obliquity and eccentricity is zero. This means that water sources and sinks need to adjust to the new boundary conditions in this run.
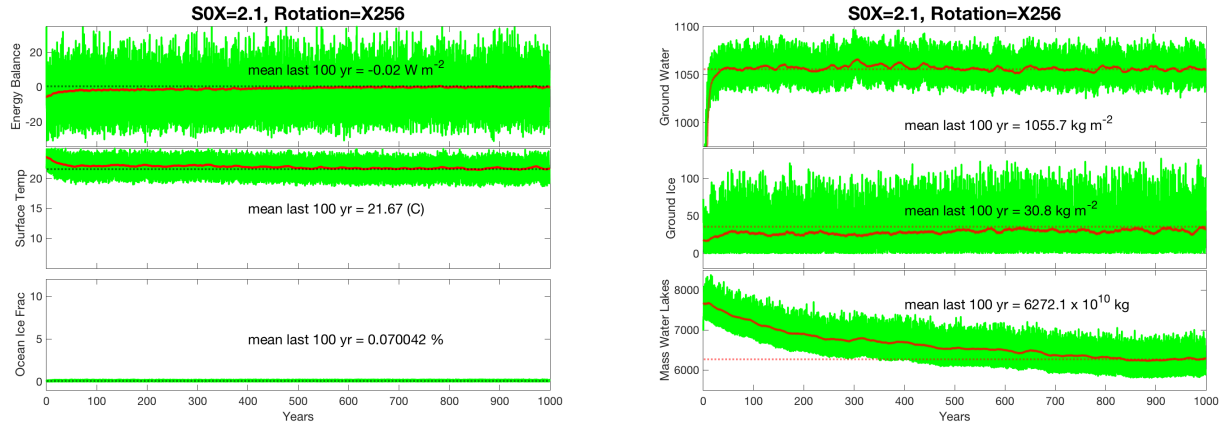
Figure 14. S0X=2.1 with sidereal day length set to 256 days (X256). Axes are the same as in Figure 13.

Figure 14a is similar to Figure 13a except that it is a world with much higher insolation (2.1 versus 1.0) and a much longer sidereal day length (X256 versus X001). The energy balance varies over a much broader range than in Figure 13a, likely due to the slower rotation rate. The surface temperature and ocean ice fraction stabilize much more quickly with the higher insolation. In Figure 14b we see a similar trend, fast stabilization for ground water, but less so for ground ice hydrologies. However, the mass of water in lakes and rivers (MWL) take nearly all 1000 years before it begins to stablize. We find that runs with longer day lengths at lower insolation take longer for MWL to come into equilibrium.

C. SIMULATIONS

Tables 8 and 9 contain the list of simulations and rundeck model configuration files available on-line. A number of boundary condition files are included in Table 10 and are also available on-line.

Table 8. Dynamic Ocean Simulations

ID	S0X[1]	SDL[2]	Mean[3]	Years[4]	Mean model output name[5]	Rundeck Name[6]
01D	1.0	X001	10	1000	ANN0990-0999.accP211eoDOFP3Od_X001_O30.nc	P211eoDOFP3Od_X001_O30.R
02D	1.0	X001	10	500	ANN0490-0499.accP211eoDOFP3OdCOND_X001_O30.nc[7]	P211eoDOFP3OdCOND_X001_O30.R
03D	1.1	X001	10	1000	ANN0990-0999.accP212eoDOFP3Od_X001_O30.nc	P212eoDOFP3Od_X001_O30.R
04D	1.2	X001	10	1300	ANN1290-1299.accP213eoDOFP3Od_X001_O30.nc	P213eoDOFP3Od_X001_O30.R
05D	1.0	X002	10	1000	ANN0990-0999.accP211eoDOFP3Od_X002_O30.nc	P211eoDOFP3Od_X002_O30.R
06D	1.1	X002	10	1000	ANN0990-0999.accP212eoDOFP3Od_X002_O30.nc	P212eoDOFP3Od_X002_O30.R
07D	1.2	X002	10	1000	ANN0990-0999.accP213eoDOFP3Od_X002_O30.nc	P213eoDOFP3Od_X002_O30.R
08D	1.0	X004	10	1000	ANN0990-0999.accP211eoDOFP3Od_X004_O30.nc	P211eoDOFP3Od_X004_O30.R
09D	1.1	X004	10	1000	ANN0990-0999.accP212eoDOFP3Od_X004_O30.nc	P212eoDOFP3Od_X004_O30.R
10D	1.2	X004	10	1000	ANN0990-0999.accP213eoDOFP3Od_X004_O30.nc	P213eoDOFP3Od_X004_O30.R
11D	1.3	X004	10	1000	ANN0990-0999.accP214eoDOFP3Od_X004_O30.nc	P214eoDOFP3Od_X004_O30.R
12D	1.0	X008	10	1000	ANN0990-0999.accP211eoDOFP3Od_X008_O30.nc	P211eoDOFP3Od_X008_O30.R
13D	1.1	X008	10	1000	ANN0990-0999.accP212eoDOFP3Od_X008_O30.nc	P212eoDOFP3Od_X008_O30.R
14D	1.2	X008	10	1000	ANN0990-0999.accP213eoDOFP3Od_X008_O30.nc	P213eoDOFP3Od_X008_O30.R
15D	1.3	X008	10	1300	ANN1290-1299.accP214eoDOFP3Od_X008_O30.nc	P214eoDOFP3Od_X008_O30.R
16D	1.4	X008	10	1500	ANN1490-1499.accP215eoDOFP3Od_X008_O30.nc	P215eoDOFP3Od_X008_O30.R
17D	1.0	X016	10	1000	ANN0990-0999.accP211eoDOFP3Od_X016_O30.nc	P211eoDOFP3Od_X016_O30.R
18D	1.1	X016	10	1000	ANN0990-0999.accP212eoDOFP3Od_X016_O30.nc	P212eoDOFP3Od_X016_O30.R
19D	1.1	X016	10	1000	ANN0990-0999.accP212eoDOFP3OdCOND_X016_O30.nc	P212eoDOFP3OdCOND_X016_O30.R
20D	1.2	X016	10	1000	ANN0990-0999.accP213eoDOFP3Od_X016_O30.nc	P213eoDOFP3Od_X016_O30.R
21D	1.3	X016	10	1000	ANN0990-0999.accP214eoDOFP3Od_X016_O30.nc	P214eoDOFP3Od_X016_O30.R
22D	1.3	X016	10	1000	ANN0990-0999.accP214eoDOFP3Od_X016_O30S.nc[8]	P214eoDOFP3Od_X016_O30S.R

Table 8 *(continued)*

ID	S0X[1]	SDL[2]	Mean[3]	Years[4]	Mean model output name[5]	Rundeck Name[6]
23D	1.4	X016	10	2200	ANN2190-2199.accP215eoDOFP3Od_X016_O30.nc	P215eoDOFP3Od_X016_O30.R
24D	1.0	X032	10	1000	ANN0990-0999.accP211eoDOFP3Od_X032_O30.nc	P211eoDOFP3Od_X032_O30.R
25D	1.1	X032	10	1000	ANN0990-0999.accP212eoDOFP3Od_X032_O30.nc	P212eoDOFP3Od_X032_O30.R
26D	1.2	X032	10	1000	ANN0990-0999.accP213eoDOFP3Od_X032_O30.nc	P213eoDOFP3Od_X032_O30.R
27D	1.3	X032	10	1300	ANN1290-1299.accP214eoDOFP3Od_X032_O30.nc	P214eoDOFP3Od_X032_O30.R
28D	1.4	X032	10	1500	ANN1490-1499.accP215eoDOFP3Od_X032_O30.nc	P215eoDOFP3Od_X032_O30.R
29D	1.5	X032	10	1500	ANN1290-1299.accP216eoDOFP3Od_X032_O30.nc	P216eoDOFP3Od_X032_O30.R
30D	1.7	X032	10	2500	ANN2490-2499.accP217eoDOFP3Od_X032_O30.nc	P217eoDOFP3Od_X032_O30.R
31D	1.9	X032	10	2500	ANN2490-2499.accP219eoDOFP3Od_X032_O30.nc	P219eoDOFP3Od_X032_O30.R
32D	2.1	X032	50	3000	ANN2950-2999.accP221eoDOFP3Od_X032_O30.nc	P221eoDOFP3Od_X032_O30.R
33D	1.0	X064	10	1000	ANN0990-0999.accP211eoDOFP3Od_X064_O30.nc	P211eoDOFP3Od_X064_O30.R
34D	1.1	X064	10	1000	ANN0990-0999.accP212eoDOFP3Od_X064_O30.nc	P212eoDOFP3Od_X064_O30.R
35D	1.2	X064	10	1000	ANN0990-0999.accP213eoDOFP3Od_X064_O30.nc	P213eoDOFP3Od_X064_O30.R
36D	1.2	X064	10	1000	ANN0990-0999.accP213eoDOFP3OdCOND_X064_O30.nc	P213eoDOFP3OdCOND_X064_O30.R
37D	1.3	X064	10	1000	ANN0990-0999.accP214eoDOFP3Od_X064_O30.nc	P214eoDOFP3Od_X064_O30.R
38D	1.4	X064	10	1000	ANN0990-0999.accP215eoDOFP3Od_X064_O30.nc	P215eoDOFP3Od_X064_O30.R
39D	1.5	X064	10	1000	ANN0990-0999.accP216eoDOFP3Od_X064_O30.nc	P216eoDOFP3Od_X064_O30.R
40D	1.7	X064	10	1000	ANN0990-0999.accP217eoDOFP3Od_X064_O30.nc	P217eoDOFP3Od_X064_O30.R
41D	1.9	X064	10	1000	ANN0990-0999.accP219eoDOFP3Od_X064_O30.nc	P219eoDOFP3Od_X064_O30.R
42D	2.1	X064	10	1000	ANN0990-0999.accP221eoDOFP3Od_X064_O30.nc	P221eoDOFP3Od_X064_O30.R
43D	2.3	X064	10	1500	ANN1490-1499.accP223eoDOFP3Od_X064_O30.nc	P223eoDOFP3Od_X064_O30.R
44D	2.5	X064	10	1700	ANN1690-1699.accP225eoDOFP3Od_X064_O30.nc	P225eoDOFP3Od_X064_O30.R
45D	2.7	X064	10	1500	ANN1490-1499.accP227eoDOFP3Od_X064_O30.nc	P227eoDOFP3Od_X064_O30.R
46D	2.9	X064	10	2000	ANN1990-1999.accP229eoDOFP3Od_X064_O30.nc	P229eoDOFP3Od_X064_O30.R
47D	1.0	X128	50	1000	ANN0950-0999.accP211eoDOFP3Od_X128_O30.nc	P211eoDOFP3Od_X128_O30.R
48D	1.1	X128	50	1000	ANN0950-0999.accP212eoDOFP3Od_X128_O30.nc	P212eoDOFP3Od_X128_O30.R
49D	1.2	X128	50	1000	ANN0950-0999.accP213eoDOFP3Od_X128_O30.nc	P213eoDOFP3Od_X128_O30.R
50D	1.3	X128	50	1000	ANN0950-0999.accP214eoDOFP3Od_X128_O30.nc	P214eoDOFP3Od_X128_O30.R
51D	1.3	X128	50	1000	ANN0950-0999.accP214eoDOFP3OdCOND_X128_O30.nc	P214eoDOFP3OdCOND_X128_O30.R
52D	1.4	X128	50	1000	ANN0950-0999.accP216eoDOFP3Od_X128_O30.nc	P215eoDOFP3Od_X128_O30.R
53D	1.5	X128	50	1000	ANN0950-0999.accP216eoDOFP3Od_X128_O30.nc	P216eoDOFP3Od_X128_O30.R
54D	1.7	X128	50	1000	ANN0950-0999.accP217eoDOFP3Od_X128_O30.nc	P217eoDOFP3Od_X128_O30.R
55D	1.9	X128	50	1000	ANN0950-0999.accP219eoDOFP3Od_X128_O30.nc	P219eoDOFP3Od_X128_O30.R
56D	2.1	X128	50	1000	ANN0950-0999.accP221eoDOFP3Od_X128_O30.nc	P221eoDOFP3Od_X128_O30.R
57D	2.3	X128	50	1000	ANN0950-0999.accP223eoDOFP3Od_X128_O30.nc	P223eoDOFP3Od_X128_O30.R
58D	2.5	X128	50	1000	ANN1250-1299.accP225eoDOFP3Od_X128_O30.nc	P225eoDOFP3Od_X128_O30.R
59D	2.7	X128	50	1000	ANN1250-1299.accP227eoDOFP3Od_X128_O30.nc	P227eoDOFP3Od_X128_O30.R
60D	1.0	X256	100	1000	ANN0900-0999.accP211eoDOFP3Od_X256_O30.nc	P211eoDOFP3Od_X256_O30.R
61D	1.0	X256	100	1000	ANN0900-0999.accP211eoDOFP3Od_X256_O30S.nc[9]	P211eoDOFP3Od_X256_O30S.R
62D	1.1	X256	100	1000	ANN0900-0999.accP212eoDOFP3Od_X256_O30.nc	P212eoDOFP3Od_X256_O30.R
63D	1.2	X256	100	1000	ANN0900-0999.accP213eoDOFP3Od_X256_O30.nc	P213eoDOFP3Od_X256_O30.R
64D	1.3	X256	100	1000	ANN0900-0999.accP214eoDOFP3Od_X256_O30.nc	P214eoDOFP3Od_X256_O30.R
65D	1.4	X256	100	1000	ANN1400-1499.accP215eoDOFP3Od_X256_O30.nc	P215eoDOFP3Od_X256_O30.R
66D	1.5	X256	100	1000	ANN0900-0999.accP216eoDOFP3Od_X256_O30.nc	P216eoDOFP3Od_X256_O30.R
67D	1.7	X256	100	1000	ANN0900-0999.accP217eoDOFP3Od_X256_O30.nc	P217eoDOFP3Od_X256_O30.R
68D	1.9	X256	100	1000	ANN0900-0999.accP219eoDOFP3Od_X256_O30.nc	P219eoDOFP3Od_X256_O30.R
69D	2.1	X256	100	1000	ANN0900-0999.accP221eoDOFP3Od_X256_O30.nc	P221eoDOFP3Od_X256_O30.R
70D	2.3	X256	100	1000	ANN0900-0999.accP223eoDOFP3Od_X256_O30.nc	P223eoDOFP3Od_X256_O30.R
71D	2.5	X256	100	1000	ANN0900-0999.accP225eoDOFP3Od_X256_O30.nc	P225eoDOFP3Od_X256_O30.R
72D	1.7	X256	100	1000	ANN0900-0999.accP225eoDOFP3Od_X256_O30S.nc[8]	P225eoDOFP3Od_X256_O30S.R

Table 8 *(continued)*

ID	S0X[1]	SDL[2]	Mean[3]	Years[4]	Mean model output name[5]	Rundeck Name[6]

[1] S0X: S0X1.0=1360.67, all other X's are multiples of 1365.3 W m^{-2}, e.g. S0X=1.1=1365.3 × 1.1 = 1501.8 W m^{-2}.

[2] SDL: Sidereal Day Length in multipules of modern Earth days (24 hours). e.g. X004 = 4 x modern Earth's sidereal day length.

[3] Mean: Number of years used for mean in column 6.

[4] Years: Length in years/orbits of model run.

[5] Filename of run on public archive. The files are averaged over the number of orbits listed in the columnn labeled "mean." To generate viewable diagnostics these netCDF files must be converted to aij, aj etc. using the ModelE2/ROCKE-3D scaleacc command. See https://simplex.giss.nasa.gov/gcm/doc/HOWTO/newio.html

[6] Name of the model configuration rundeck file.

[7] COND in name indicates "convective condensate precipitates" in this particular run. See Section 3.2.

[8] S at end of this name indicates soil is 100% loam/silt.

[9] S at end of this name indicates soil is 100% sand.

Table 9. Q-flux=0 Ocean Simulations

ID	S0X	SDL	Mean	Years	Mean model output name	Rundeck name
01Z	1.0	X001B[1]	10	200	ANN0190-0199.accP211eoZoht100_X001B_O30.nc	P211eoZoht100_X001B_O30.R
02Z	1.1	X001B	10	200	ANN0190-0199.accP212eoZoht100_X001B_O30.nc	P212eoZoht100_X001B_O30.R
03Z	1.2	X001B	10	200	ANN0190-0199.accP213eoZoht100_X001B_O30.nc	P213eoZoht100_X001B_O30.R
04Z	1.3	X001B	10	200	ANN0190-0199.accP214eoZoht100_X001B_O30.nc	P214eoZoht100_X001B_O30.R
05Z	1.0	X001	10	200	ANN0190-0199.accP211eoZoht100_X001_O30.nc	P211eoZoht100_X001B_O30.R
06Z	1.0	X001	10	200	ANN0190-0199.accP211eoZoht100COND_X001_O30.nc	P211eoZoht100COND_X001B_O30.R
07Z	1.1	X001	10	200	ANN0190-0199.accP212eoZoht100_X001_O30.nc	P212eoZoht100_X001B_O30.R
08Z	1.2	X001	10	200	ANN0190-0199.accP213eoZoht100_X001_O30.nc	P213eoZoht100_X001B_O30.R
109Z	1.0	X002	10	200	ANN0190-0199.accP211eoZoht100_X002_O30.nc	P211eoZoht100_X002_O30.R
10Z	1.1	X002	10	200	ANN0190-0199.accP212eoZoht100_X002_O30.nc	P212eoZoht100_X002_O30.R
11Z	1.2	X002	10	200	ANN0190-0199.accP213eoZoht100_X002_O30.nc	P213eoZoht100_X002_O30.R
12Z	1.3	X002	10	200	ANN0190-0199.accP214eoZoht100_X002_O30.nc	P214eoZoht100_X002_O30.R
13Z	1.4	X002	10	200	ANN0190-0199.accP215eoZoht100_X002_O30.nc	P215eoZoht100_X002_O30.R
14Z	1.0	X004	10	200	ANN0190-0199.accP211eoZoht100_X004_O30.nc	P211eoZoht100_X004_O30.R
15Z	1.1	X004	10	200	ANN0190-0199.accP212eoZoht100_X004_O30.nc	P212eoZoht100_X004_O30.R
16Z	1.2	X004	10	200	ANN0190-0199.accP213eoZoht100_X004_O30.nc	P213eoZoht100_X004_O30.R
17Z	1.3	X004	10	200	ANN0190-0199.accP214eoZoht100_X004_O30.nc	P214eoZoht100_X004_O30.R
18Z	1.0	X008	10	200	ANN0190-0199.accP211eoZoht100_X008_O30.nc	P211eoZoht100_X008_O30.R
19Z	1.1	X008	10	200	ANN0190-0199.accP212eoZoht100_X008_O30.nc	P212eoZoht100_X008_O30.R
20Z	1.2	X008	10	200	ANN0190-0199.accP213eoZoht100_X008_O30.nc	P213eoZoht100_X008_O30.R
21Z	1.3	X008	10	200	ANN0190-0199.accP214eoZoht100_X008_O30.nc	P214eoZoht100_X008_O30.R
22Z	1.4	X008	10	200	ANN0190-0199.accP215eoZoht100_X008_O30.nc	P215eoZoht100_X008_O30.R
23Z	1.0	X016	10	200	ANN0190-0199.accP211eoZoht100_X016_O30.nc	P211eoZoht100_X016_O30.R
24Z	1.1	X016	10	200	ANN0190-0199.accP212eoZoht100_X016_O30.nc	P212eoZoht100_X016_O30.R
25Z	1.1	X016	10	200	ANN0190-0199.accP212eoZoht100COND_X016_O30.nc	P212eoZoht100COND_X016_O30.R
26Z	1.2	X016	10	200	ANN0190-0199.accP213eoZoht100_X016_O30.nc	P213eoZoht100_X016_O30.R
27Z	1.3	X016	10	200	ANN0190-0199.accP214eoZoht100_X016_O30.nc	P214eoZoht100_X016_O30.R
28Z	1.4	X016	10	200	ANN0190-0199.accP215eoZoht100_X016_O30.nc	P215eoZoht100_X016_O30.R
29Z	1.5	X016	10	200	ANN0190-0199.accP216eoZoht100_X016_O30.nc	P216eoZoht100_X016_O30.R
30Z	1.0	X032	10	200	ANN0190-0190.accP211eoZoht100_X032_O30.nc	P211eoZoht100_X032_O30.R
31Z	1.1	X032	10	200	ANN0190-0190.accP212eoZoht100_X032_O30.nc	P212eoZoht100_X032_O30.R
32Z	1.2	X032	10	200	ANN0190-0190.accP213eoZoht100_X032_O30.nc	P213eoZoht100_X032_O30.R
33Z	1.3	X032	10	200	ANN0190-0199.accP214eoZoht100_X032_O30.nc	P214eoZoht100_X032_O30.R
34Z	1.4	X032	10	200	ANN0190-0199.accP215eoZoht100_X032_O30.nc	P215eoZoht100_X032_O30.R

Table 9 *(continued)*

ID	S0X	SDL	Mean	Years	Mean model output name	Rundeck name
35Z	1.5	X032	10	200	ANN0190-0199.accP216eoZoht100_X032_O30.nc	P216eoZoht100_X032_O30.R
36Z	1.7	X032	10	200	ANN0190-0199.accP217eoZoht100_X032_O30.nc	P217eoZoht100_X032_O30.R
37Z	1.9	X032	10	400	ANN0390-0399.accP219eoZoht100_X032_O30.nc	P219eoZoht100_X032_O30.R
38Z	1.0	X064	10	200	ANN0190-0190.accP211eoZoht100_X064_O30.nc	P211eoZoht100_X064_O30.R
39Z	1.1	X064	10	200	ANN0190-0190.accP212eoZoht100_X064_O30.nc	P212eoZoht100_X064_O30.R
40Z	1.2	X064	10	200	ANN0190-0190.accP213eoZoht100_X064_O30.nc	P213eoZoht100_X064_O30.R
41Z	1.2	X064	10	200	ANN0190-0190.accP213eoZoht100COND_X064_O30.nc	P213eoZoht100COND_X064_O30.R
42Z	1.3	X064	10	200	ANN0190-0190.accP214eoZoht100_X064_O30.nc	P214eoZoht100_X064_O30.R
43Z	1.4	X064	10	200	ANN0190-0190.accP215eoZoht100_X064_O30.nc	P215eoZoht100_X064_O30.R
44Z	1.5	X064	10	200	ANN0190-0190.accP216eoZoht100_X064_O30.nc	P216eoZoht100_X064_O30.R
45Z	1.7	X064	10	200	ANN0190-0190.accP217eoZoht100_X064_O30.nc	P217eoZoht100_X064_O30.R
46Z	1.9	X064	10	200	ANN0190-0190.accP219eoZoht100_X064_O30.nc	P219eoZoht100_X064_O30.R
47Z	2.1	X064	10	200	ANN0190-0190.accP221eoZoht100_X064_O30.nc	P221eoZoht100_X064_O30.R
48Z	2.3	X064	10	200	ANN0190-0199.accP223eoZoht100_X064_O30.nc	P223eoZoht100_X064_O30.R
49Z	2.5	X064	10	200	ANN0190-0199.accP225eoZoht100_X064_O30.nc	P225eoZoht100_X064_O30.R
50Z	2.7	X064	10	200	ANN0190-0199.accP227eoZoht100_X064_O30.nc	P227eoZoht100_X064_O30.R
51Z	2.9	X064	10	200	ANN0190-0199.accP229eoZoht100_X064_O30.nc	P229eoZoht100_X064_O30.R
52Z	1.0	X128	50	200	ANN0150-0199.accP211eoZoht100_X128_O30.nc	P211eoZoht100_X128_O30.R
53Z	1.1	X128	50	200	ANN0150-0199.accP212eoZoht100_X128_O30.nc	P212eoZoht100_X128_O30.R
54Z	1.2	X128	50	200	ANN0150-0199.accP213eoZoht100_X128_O30.nc	P213eoZoht100_X128_O30.R
55Z	1.3	X128	50	200	ANN0150-0199.accP214eoZoht100_X128_O30.nc	P214eoZoht100_X128_O30.R
56Z	1.3	X128	50	200	ANN0150-0199.accP214eoZoht100COND_X128_O30.nc	P214eoZoht100COND_X128_O30.R
57Z	1.4	X128	50	200	ANN0150-0199.accP215eoZoht100_X128_O30.nc	P215eoZoht100_X128_O30.R
58Z	1.5	X128	50	200	ANN0150-0199.accP216eoZoht100_X128_O30.nc	P216eoZoht100_X128_O30.R
59Z	1.7	X128	50	200	ANN0150-0199.accP217eoZoht100_X128_O30.nc	P217eoZoht100_X128_O30.R
60Z	1.9	X128	50	200	ANN0150-0199.accP219eoZoht100_X128_O30.nc	P219eoZoht100_X128_O30.R
61Z	2.1	X128	50	200	ANN0150-0199.accP221eoZoht100_X128_O30.nc	P221eoZoht100_X128_O30.R
62Z	2.3	X128	50	200	ANN0150-0199.accP223eoZoht100_X128_O30.nc	P223eoZoht100_X128_O30.R
63Z	2.5	X128	50	200	ANN0150-0199.accP225eoZoht100_X128_O30.nc	P225eoZoht100_X128_O30.R
64Z	2.7	X128	50	200	ANN0150-0199.accP227eoZoht100_X128_O30.nc	P227eoZoht100_X128_O30.R
65Z	1.0	X256	100	200	ANN0100-0199.accP211eoZoht100_X256_O30.nc	P211eoZoht100_X256_O30.R
66Z	1.1	X256	100	200	ANN0100-0199.accP212eoZoht100_X256_O30.nc	P212eoZoht100_X256_O30.R
67Z	1.2	X256	100	200	ANN0100-0199.accP213eoZoht100_X256_O30.nc	P213eoZoht100_X256_O30.R
68Z	1.3	X256	100	200	ANN0100-0199.accP214eoZoht100_X256_O30.nc	P214eoZoht100_X256_O30.R
69Z	1.4	X256	100	200	ANN0100-0199.accP215eoZoht100_X256_O30.nc	P215eoZoht100_X256_O30.R
70Z	1.5	X256	100	200	ANN0100-0199.accP216eoZoht100_X256_O30.nc	P216eoZoht100_X256_O30.R
71Z	1.7	X256	100	200	ANN0100-0199.accP217eoZoht100_X256_O30.nc	P217eoZoht100_X256_O30.R
72Z	1.9	X256	100	200	ANN0100-0199.accP219eoZoht100_X256_O30.nc	P219eoZoht100_X256_O30.R
73Z	2.1	X256	100	200	ANN0100-0199.accP221eoZoht100_X256_O30.nc	P221eoZoht100_X256_O30.R
74Z	2.3	X256	100	200	ANN0100-0199.accP223eoZoht100_X256_O30.nc	P223eoZoht100_X256_O30.R
75Z	2.5	X256	100	200	ANN0100-0199.accP225eoZoht100_X256_O30.nc	P225eoZoht100_X256_O30.R

[1] B at end of name indicates radiation balance set to colder temperatures via cloud tuning. See Section 3.2 for details.

REFERENCES

Abbot, D. S., Cowan, N. B., & Ciesla, F. J. 2012, ApJ, 756, 178

Allison, M., Del Genio, A. D., & Zhou, W. 1995, Geophysical Research Letters, 22, 2957. http://dx.doi.org/10.1029/95GL02818

Table 10. Boundary Condition Files[1]

Name[2]	Input filename[3]	Description
AIC.RES_M20A.D771201_40L.nc	AIC	Atmosphere Initial Conditions
GIC.E046D3M20A.1DEC1955.ext_1.nc	GIC	Ground Initial Conditions
Z72X46N_gas.1_nocasp_btub005.nc	TOPO	Land Topography
OZ72X46N_gas.1_nocasp_btub005.nc	TOPO_OC	Dynamic Ocean Topography[4]
OIC4X5LD.Z12.gas1.CLEV94.DEC01_btub00.nc	OIC	Ocean Initial Conditions
OSTRAITS_72x46btub0.nml	OSTRAITS	Ocean Straits[4]
RD_modelE_M_btub004D.nc	RVR	River Directions[4]
RD_modelE_M.names_btub0.txt	NAMERVR	River Names[4]
zero_OHT_4x5_100m.nc	OHT	Q-flux=0 Ocean Heat Transport[5]
zero_OCNML_4x5_100m.nc	OCNML	Q-flux=0 initial ocean layer depth[5]
V72X46.1.cor2_no_crops02.ext.nc	VEG	Uniform surface albedo=0.2
S4X50093SANDCLAY.ext.nc	SOIL	Soil Type (50/50 sand/clay)
S4X50093LOAM.ext.nc	SOIL	Soil Type (100% loam/silt)
S4X50093SAND.ext.nc	SOIL	Soil Type (100% sand)
GLMELT_4X5.OCN_MWAY0.nc	GLMELT	Glacial Melt Areas
GHG.MWAY201412B.txt	GHG	Green House Gas concentrations

[1] These files may be downloaded from https://portal.nccs.nasa.gov/GISS_modelE/ROCKE-3D and/or The Internet Archive https://archive.org/details/Climates_of_Warm_Earth_like_Planets

[2] Files ending in nc are formatted in NetCDF (https://www.unidata.ucar.edu/software/netcdf/), NetCDF is software developed by UCAR/Unidata http://doi.org/10.5065/D6H70CW6. Non-nc files are simple flat text files.

[3] The name for the assignment variable in ROCKE-3D.

[4] Fully Coupled Dynamic Ocean input files.

[5] This file is used for Q-flux=0 oceans of 100m depth.

Boutle, I. A., Mayne, N. J., Drummond, B., et al. 2017, A&A, 601, A120

Cess, R., Potter, G., Blanchet, J., et al. 1990, Journal of Geophysical Research: Atmospheres, 95, 16601

Charnay, B., Forget, F., Wordsworth, R., et al. 2013, Journal of Geophysical Research (Atmospheres), 118, 10

Charnay, B., Le Hir, G., Fluteau, F., Forget, F., & Catling, D. C. 2017, Earth and Planetary Science Letters, 474, 97

Checlair, J., Menou, K., & Abbot, D. S. 2017, ApJ, 845, 132

Codron, F. 2012, Climate Dynamics, 38, 379. https://doi.org/10.1007/s00382-011-1031-3

Cullum, J., Stevens, D., & Joshi, M. 2014, Astrobiology, 14, 645

Del Genio, A. D. 2013, in Comparative Climatology of Terrestrial Planets, ed. S. J. Mackwell, A. A. Simon-Miller, J. W. Harder, & M. A. Bullock, Space Science Series (Phoenix: University of Arizona Press), 3–18

Del Genio, A. D. 2015, ArXiv e-prints, arXiv:1603.07424

Del Genio, A. D., Kovari, W., Yao, M. S., & Jonas, J. 2005, Journal of Climate, 18, 2386

Del Genio, A. D., & Suozzo, R. J. 1987, Journal of Atmospheric Sciences, 44, 973

Del Genio, A. D., Way, M. J., Amundsen, D. S., et al. 2018, ArXiv e-prints, arXiv:1709.02051

Del Genio, A. D., Yao, M.-S., & Jonas, J. 2007, Geophysical Research Letters, 34, doi:10.1029/2007GL030525

Del Genio, A. D., Zhou, W., & Eichler, T. P. 1993, Icarus, 101, 1

Edson, A., Lee, S., Bannon, P., Kasting, J. F., & Pollard, D. 2011, Icarus, 212, 1

Edson, A. R., Kasting, J. F., Pollard, D., Lee, S., & Bannon, P. R. 2012, Astrobiology, 12, 562

Edwards, J. M. 1996, Journal of Atmospheric Sciences, 53, 1921

Edwards, J. M., & Slingo, A. 1996, Quarterly Journal of the Royal Meteorological Society, 122, 689

Elsaesser, G. S., Del Genio, A. D., Jiang, J. H., & van Lier-Walqui, M. 2017, Journal of Climate, 30, 317

Farneti, R., & Vallis, G. K. 2011, Climate Dynamics, 36, 289. http://dx.doi.org/10.1007/s00382-009-0674-9

Ferreira, D., Marshall, J., O'Gorman, P. A., & Seager, S. 2014, Icarus, 243, 236

Forget, F. 1998, Earth Moon and Planets, 81, 59

Forster, P. M., Andrews, T., Good, P., et al. 2013, Journal of Geophysical Research: Atmospheres, 118, 1139. https://agupubs.onlinelibrary.wiley.com/doi/abs/10.1002/jgrd.50174

26

Fu, R., Del Genio, A. D., & Rossow, W. B. 1990, J. Climate, 3, 1129

Fujii, Y., Del Genio, A. D., & Amundsen, D. S. 2017, ApJ, 848, 100

Gent, P. R., & McWilliams, J. C. 1990, Journal of Physical Oceanography, 20, 150

Godolt, M., Grenfell, J. L., Hamann-Reinus, A., et al. 2015, Planet. Space Sci., 111, 62

Goldblatt, C., Robinson, T. D., Zahnle, K. J., & Crisp, D. 2013, Nature Geoscience, 6, 661

Hart, M. H. 1979, Icarus, 37, 351

Hu, Y., & Yang, J. 2014, Proceedings of the National Academy of Science, 111, 629

Joshi, M. 2003, Astrobiology, 3, 415

Joshi, M. M., Haberle, R. M., & Reynolds, R. T. 1997, Icarus, 129, 450

Jury, W., Gardner, W., & Gardner, W. 1991, Soil Physics (J. Wiley).
https://books.google.se/books?id=0HJRAAAAMAAJ

Kasting, J. F., Whitmire, D. P., & Reynolds, R. T. 1993, Icarus, 101, 108

Kiang, N. K., Way, M. J., Del Genio, A. D., et al. 2018, ApJ

Kilic, C., Lunkeit, F., Raible, C. C., & Stocker, T. F. 2018, ApJ, 864, 106

Kilic, C., Raible, C. C., & Stocker, T. F. 2017, ApJ, 844, 147

Klein, S. A., Hall, A., Norris, J. R., & Pincus, R. 2017, Surveys in Geophysics, 38, 1307.
https://doi.org/10.1007/s10712-017-9433-3

Kopparapu, R. K., Ramirez, R. M., SchottelKotte, J., et al. 2014, ApJL, 787, L29

Kopparapu, R. K., Wolf, E. T., Haqq-Misra, J., et al. 2016, The Astrophysical Journal, 819, 84

Kopparapu, R. K., Ramirez, R., Kasting, J. F., et al. 2013, ApJ, 765, 131

Leconte, J., Forget, F., Charnay, B., Wordsworth, R., & Pottier, A. 2013a, Nature, 504, 268

Leconte, J., Forget, F., Charnay, B., et al. 2013b, A&A, 554, A69

Madeleine, J.-B., Forget, F., Head, J. W., et al. 2014, in Mars Atmosphere: Modelling and Observation, 5th International Workshop, ed. F. Forget & M. Millour, 4102

Mauritsen, T., Stevens, B., Roeckner, E., et al. 2012, Journal of Advances in Modeling Earth Systems, 4, doi:10.1029/2012MS000154

Merlis, T. M., & Schneider, T. 2010, Journal of Advances in Modeling Earth Systems, 2, 13

Navarra, A., & Boccaletti, G. 2002, Climate Dynamics, 19, 467. http://dx.doi.org/10.1007/s00382-002-0238-8

Noda, S., Ishiwatari, M., Nakajima, K., et al. 2017, Icarus, 282, 1

Pierrehumbert, R., & Gaidos, E. 2011, ApJL, 734, L13

Pierrehumbert, R. T. 2011, ApJL, 726, L8

Popp, M., & Eggl, S. 2017, Nature Communications, 8, 14957

Popp, M., Schmidt, H., & Marotzke, J. 2013, in EGU General Assembly Conference Abstracts, Vol. 15, EGU General Assembly Conference Abstracts, EGU2013–4852

Popp, M., Schmidt, H., & Marotzke, J. 2016, Nature Communications, 7, 10627

Ramirez, R. M., & Kaltenegger, L. 2014, ApJL, 797, L25

Rothman, L. S., Gordon, I. E., Babikov, Y., et al. 2013, JQSRT, 130, 4

Russell, G. L., Lacis, A. A., Rind, D. H., Colose, C., & Opstbaum, R. F. 2013, Geophysical Research Letters, 40, 5787, 2013GL056755.
http://dx.doi.org/10.1002/2013GL056755

Russell, G. L., Miller, J. R., & Rind, D. 1995, Atmosphere-Ocean, 33, 683.
http://dx.doi.org/10.1080/07055900.1995.9649550

Russell, G. L., Miller, J. R., & Tsang, L.-C. 1985, Dynamics of Atmospheres and Oceans, 9, 253

Salameh, J., Popp, M., & Marotzke, J. 2018, Climate Dynamics, 50, 2395.
https://doi.org/10.1007/s00382-017-3548-6

Schmidt, G. A., Kelley, M., Nazarenko, L., et al. 2014, Journal of Advances in Modeling Earth Systems, 6, 141.
http://dx.doi.org/10.1002/2013MS000265

Selsis, F., Kasting, J. F., Levrard, B., et al. 2007, A&A, 476, 1373

Shields, A. L., Bitz, C. M., Meadows, V. S., Joshi, M. M., & Robinson, T. D. 2014, ApJL, 785, L9

Shields, A. L., Meadows, V. S., Bitz, C. M., et al. 2013, Astrobiology, 13, 715

Showman, A. P., Lewis, N. K., & Fortney, J. J. 2015, ApJ, 801, 95

Showman, A. P., Wordsworth, R. D., Merlis, T. M., & Kaspi, Y. 2013, Comparative Climatology of Terrestrial Planets, 277

Soden, B. J., & Held, I. M. 2006, Journal of Climate, 19, 3354. https://doi.org/10.1175/JCLI3799.1

Spiegel, D. S., Menou, K., & Scharf, C. A. 2008, ApJ, 681, 1609

Stone, P. H. 1978, Dynamics of Atmospheres and Oceans, 2, 123 . http://www.sciencedirect.com/science/article/pii/0377026578900064

Turbet, M., Leconte, J., Selsis, F., et al. 2016, A&A, 595, A112

Vial, J., Dufresne, J.-L., & Bony, S. 2013, Climate Dynamics, 41, 3339. https://doi.org/10.1007/s00382-013-1725-9

Way, M. J., Del Genio, A. D., Kelley, M., Aleinov, I., & Clune, T. 2015, ArXiv e-prints, arXiv:1511.07283

Way, M. J., Del Genio, A. D., Kiang, N. Y., et al. 2016, Geophys. Res. Lett., 43, 8376

Way, M. J., & Georgakarakos, N. 2017, ApJL, 835, L1

Way, M. J., Aleinov, I., Amundsen, D. S., et al. 2017, ApJS, 231, 12

Williams, G. P., & Holloway, J. L. 1982, Nature, 297, 295

Wolf, E. T., & Toon, O. B. 2013, Astrobiology, 13, 656

—. 2015, Journal of Geophysical Research (Atmospheres), 120, 5775

Yang, J., Boué, G., Fabrycky, D. C., & Abbot, D. S. 2014, ApJL, 787, L2

Yang, J., Cowan, N. B., & Abbot, D. S. 2013, ApJL, 771, L45

Yang, J., Peltier, W. R., & Hu, Y. 2012a, Journal of Climate, 25, 2711. https://doi.org/10.1175/JCLI-D-11-00189.1

—. 2012b, Journal of Climate, 25, 2737. https://doi.org/10.1175/JCLI-D-11-00190.1